Accepted manuscript version – Geochimica et Cosmochimica Acta (v. 356, Sep 2023, 129-148) https://doi.org/10.1016/j.gca.2023.07.009

The magmatic-hydrothermal transition in P-rich pegmatitic melts: crystal-melt-fluid interactions recorded by phosphate minerals

Fernando Prado Araujo[a*], Philippe Muchez[a], and Niels Hulsbosch[a]

[a]KU Leuven, Department of Earth and Environmental Sciences, Division of Geology. Celestijnenlaan 200E - Box 2410, 3001 Leuven, Belgium (*corresponding author: fernando.pradoaraujo@kuleuven.be)

ABSTRACT

Rare-element pegmatites are the crystallization product of melts strongly enriched in incompatible elements. Some of these elements, e.g., Li, B, P, F, and H_2O, function as melt structure modifiers, allowing such melts to reach unusually low crystallization temperatures and regulating the saturation of aqueous-carbonic fluids from the melt. However, the timing of fluid saturation is highly debated, and the processes that mark the magmatic-hydrothermal transition in rare-element pegmatites are still elusive. The crystallization sequence of phosphate minerals can be used to assess the timing and nature of fluid-related processes in pegmatitic systems. In the Buranga pegmatite, western Rwanda, magmatic phosphates are replaced by (hydrous) alkali-rich phosphates and later by strongly hydrated phosphates as the dike cools. This reaction series indicates a disequilibrium in the crystal-melt-fluid system and records complex fluid-rock interactions during dike consolidation. This contribution compares these interactions with the fluid record preserved in fluid inclusions in the main phosphates of the crystallization sequence. Three major fluid inclusion types are observed, aqueous-carbonic (mostly two-phase, L-V), carbonic-aqueous (two-phase, V-L, or three-phase, L-L-V), and crystal-rich inclusions (multiphase, L-V-Solids). Crystal-rich fluid inclusions in trolleite [$Al_4(PO_4)_3(OH)_3$], the last primary phosphate to precipitate from the melt, show a paragenesis of solid phases similar to the secondary phosphates observed in the dike. LA-ICPMS analyses of individual fluid inclusions show high concentrations of Na and K, with some content of Li, Rb, Cs, B, Fe, and Mn in the fluid. A similar composition is present in all inclusion types within the same mineral. Crystal-rich fluid inclusions demonstrate that during the magmatic-hydrothermal transition, primary phosphates react with the fluid in the presence of melt to generate secondary phosphates. No evidence

of external fluid sources has been observed during the magmatic-hydrothermal transition. The fluid inclusion record shows that the fluid salinity is kept constant due to fluid-mineral interactions and corroborates the hypothesis that fluid-soluble elements are internally remobilized in the melt-crystal-fluid system during the magmatic-hydrothermal stage. These interpretations have implications for the general evolution of P-rich pegmatitic melts and the mineralization of Nb and Ta in these systems.

Keywords: Pegmatite, fluid inclusions, crystal-rich inclusions, Buranga, fluid-rock interactions

1. INTRODUCTION

Rare-element pegmatites represent the crystallization product of highly differentiated granitic melts. These melts are frequently interpreted as either residual liquids extracted from larger granite mushes (Černý et al., 1985; Simmons and Webber, 2008; Roda-Robles et al., 2012b; Thomas and Davidson, 2013; Hulsbosch et al., 2014; London, 2022), or products of partial melting of crustal materials in migmatitic terranes (Barros and Menuge, 2016; Müller et al., 2017; Fuchsloch et al., 2018; Shaw et al., 2022). In both cases, rare-element pegmatites are strongly enriched in incompatible elements, some of which (e.g., Li, B, P, F, and H, as H_2O or OH^- groups) also act as melt structure modifiers. The concentration of these elements, also referred to as fluxing components, in the melt significantly affects the properties of pegmatitic magmas.

Fluxes depolymerize the melt structure and thus enhance the miscibility of H_2O in the melt (Holtz et al., 1993; London et al., 1993; Dingwell et al., 1997; Behrens et al., 2001), decrease its liquidus temperature and viscosity (London, 1987; Dingwell et al., 1993; Bartels et al., 2011), and boost crystal growth over nucleation (Simmons and Webber, 2008; Nabelek et al., 2010). Additionally, a high content of fluxing components is normally invoked to explain the persistence of pegmatitic melts well below their equilibrium liquidus temperature (Sirbescu and Nabelek, 2003a; Gammel and Nabelek, 2016).

The lowered liquidus temperature and increased water solubility of flux-rich pegmatitic melts may delay the immiscibility of a (hydrosaline) fluid phase from the melt (Pichavant, 1983; London, 1986; Dingwell et al., 1997; Behrens et al., 2001; Nabelek et al., 2010). Consequently, the stage where

crystals, melt, and fluid coexist (i.e., magmatic-hydrothermal stage) may vary in each pegmatite intrusion depending on its composition and crystallization path.

Overall, the magmatic-hydrothermal transition in pegmatites, marked by the exsolution of an aqueous (-carbonic) fluid, is debated to be either: 1) a continuum between the magmatic (melt-dominated) and hydrothermal (fluid-dominated) stages occurring throughout the pegmatite crystallization (Jahns and Burnham, 1969); 2) a sharp transition marked by melt-melt-fluid immiscibility processes from a supercritical hydrosilicate fluid after pegmatite emplacement (Thomas and Davidson, 2016); 3) occurring very late during pegmatite consolidation (e.g., miarolitic stage), essentially near or at subsolidus conditions after extensive crystallization of fluid-undersaturated melts (Cameron et al., 1949; London, 2022). A key conundrum of this discussion is whether an aqueous fluid exsolves from the melt, when it does, and as such, if it forms an integral part of the crystallization history of pegmatites.

Fluid saturation from a melt before complete crystallization has been demonstrated for rare-metal granites (Michaud and Pichavant, 2020), rare-element pegmatites (Hulsbosch and Muchez, 2020), and even P-rich pegmatites (Siegel et al., 2016). However, the timing of such immiscibility processes is highly debated (London, 2015; Thomas and Davidson, 2015), and the processes taking place at the magmatic-hydrothermal transition in natural flux-rich pegmatites are still unclear, especially for P-rich melts. Fluid saturation in rare-element pegmatites is shown to occur early, from the crystallization of wall and intermediate zones (Lu and Lottermoser, 1997; Beurlen et al., 2001; Sirbescu and Nabelek, 2003b; Mulja and Williams-Jones, 2018) with indications that it is locally controlled by rapid growth of coarse-grained crystals (Sirbescu et al., 2017; Hulsbosch and Muchez, 2020).

Contrarily, other studies interpret an intermediate to late exsolution (Alfonso and Melgarejo, 2008; Gammel and Nabelek, 2016; Ashworth et al., 2018; Michallik et al., 2020), possibly near subsolidus conditions (London, 1986). This interpretation is validated by trace element and isotopic analyses in rare-metal granites, showing that a single magmatic fluid can generate the observed geochemical patterns without requiring a melt-melt immiscibility (Michaud and Pichavant, 2020).

Late fluid exsolution from the melt is also invoked to explain tourmaline compositional variations and isotopic data in P-rich pegmatites (Siegel et al., 2016). Furthermore, the near solidus fluid exsolution in granite-pegmatite systems is often connected with the formation of late replacement textures, such as growth of secondary muscovite (greisenization/muscovitization) (Pollard et al., 1991; Bettencourt et al., 2005; Hulsbosch and Muchez, 2020).

Phosphate minerals and their paragenesis can be used to constrain the timing and nature of immiscibility processes in pegmatitic melts. They are sensitive to physicochemical changes during crystallization and are important records of the internal fractionation (London and Burt, 1982; London et al., 2001; Llorens and Moro, 2012; Harlov, 2015; Rao et al., 2017). Pegmatitic phosphates are frequently subdivided into 1) primary, crystallized from the melt at a magmatic stage; 2) metasomatic, formed by high-temperature replacement of magmatic phases during the transition from a melt- to a fluid-dominated environment; and 3) hydrothermal, generated by late-stage solutions under subsolidus to supergene conditions (Fisher, 1958; Moore, 1973; Fransolet et al., 1986; Roda et al., 2004; Baijot et al., 2014; Włodek et al., 2015; Galliski et al., 2020). Each of those stages is usually associated with specific geochemical processes within the crystal-melt-fluid system, such as enrichment of incompatible elements (e.g., Li, Rb, Cs, etc.), remobilization of soluble elements (e.g., Na, Ca, F, etc.), and strong oxidation and hydration, respectively (Fisher, 1958; Moore, 1973; Pirard et al., 2007; Roda-Robles et al., 2010; Baijot et al., 2014).

The crystallization/resorption of phosphate minerals also directly affects the concentration of fluxes (P, Li, F, and OH) and other relevant elements in the melt, such as Na, Ca, Fe, and Mn. It is proposed that phosphates buffer the Fe and Mn content of P-rich melts, preventing the precipitation of columbite-group minerals until the earlier Fe-Mn-bearing oxide, silicate, and phosphate phases are destabilized under fluid-present conditions and Fe and Mn are released back to the crystal-melt-fluid system (Linnen et al., 2019; McNeil et al., 2020; Prado Araujo et al., 2023). Interactions between a fluid phase and either the paragenetically early minerals or the melt during cooling of the intrusion are suggested by most studies on pegmatitic phosphates (London and Burt, 1982; Roda et al., 2004; Galliski et al., 2012; Baijot et al., 2014). However, the properties and compositional evolution of such

fluid phase were never directly characterized for natural pegmatite systems and the fluid phase that was present during the crystallization and alteration of phosphate minerals remains a speculative entity.

The P-rich rare-element Buranga pegmatite, located in the Gatumba Pegmatite District of western Rwanda, is a remarkable natural example to assess the relationship between the crystallization of phosphate mineral assemblages, immiscibility processes, melt-crystal-fluid interactions, and Nb-Ta mineralization in pegmatitic melts. The dike is a highly evolved LCT pegmatite known for its outstanding occurrence of phosphate minerals, presenting more than 50 species (Daltry and von Knorring, 1998) and being the type locality for bertossaite [$(Li,Na)_2(Ca,Fe^{2+},Mn^{2+})Al_4(PO_4)_4(OH,F)_4$], burangaite [$NaFe^{2+}Al_5(PO_4)_4(OH)_6.2H_2O$] and gatumbaite [$CaAl_2(PO_4)_2(OH)_2.H_2O$]. Additionally, it currently hosts artisanal exploitations of columbite-group minerals and cassiterite in the weathered zones (Dewaele et al., 2011; Muchez et al., 2014). Previous studies in the Buranga dike described specific assemblages of phosphate minerals for each of the magmatic, magmatic-hydrothermal, and hydrothermal crystallization stages and showed that columbite-group minerals' mineralization is related to the fluid-induced breakdown of primary phosphates minerals at the magmatic-hydrothermal stage (Prado Araujo et al., 2023). However, the composition of the fluid phase(s) involved is still elusive. The integration of the phosphate paragenesis with the specific crystallization conditions of each mineral and the fluid evolution recorded by fluid inclusions within them can reveal the chemical evolution of the pegmatite system and constrain the late stages of consolidation in the Buranga dike, contributing to the ongoing discussion on the magmatic-hydrothermal transition in pegmatites.

This contribution investigates the fluid inclusion record in the main phosphate minerals from the magmatic and magmatic-hydrothermal crystallization stages defined by Prado Araujo et al. (2023) to reconstruct the fluid compositional evolution during the magmatic-hydrothermal transition in the Buranga pegmatite and determine the crystal-melt-fluid interactions taking place during this transition. Additionally, the role of this fluid evolution and fluid-rock interaction on the crystallization of Nb-Ta-oxide minerals in flux-rich rare-element pegmatites is discussed.

2. GEOLOGICAL SETTING

2.1. *Regional context*

The study area is located in the Karagwe-Ankole Belt (KAB) of Central Africa (Tack et al., 2010; Fernandez-Alonso et al., 2012; Van Daele et al., 2020). The many pegmatite fields documented in the region are linked to the early Neoproterozoic "Kibara tin granites" (Pohl et al., 2013; Melcher et al., 2015; Hulsbosch, 2019). The Gitarama-Gatumba field is one of the best representatives of the Ta-Nb-Sn-W-Li mineralization within the province (Dewaele et al., 2011; Hulsbosch et al., 2014; Hulsbosch et al., 2016). It encompasses pegmatite dikes spatially zoned around S-type batholiths following a magmatic fractionation trend (Varlamoff, 1972; Muchez et al., 2014). The highly fractionated residual melts are represented by the Nb-Ta-Sn-mineralized pegmatites, which are also enriched in Li, Be, B, and P (Hulsbosch et al., 2014).

2.2. *Buranga pegmatite*

The Buranga pegmatite is a phosphorus-rich dike from the LCT family. It is one of the Nb-Ta-Sn-mineralized pegmatites in the Gitarama-Gatumba field, but its exceptionality comes from the more than 50 phosphate minerals described in the dike (Daltry and von Knorring, 1998). Phosphate minerals occur as polymineralic nodules in the quartz-dominated core zone and the transition region between the intermediate and core zones (Fransolet, 1975). Two groups of phosphate nodules were described in Buranga (Polinard, 1950): (1) massive blocks of several cubic decimeters dominated by white montebrasite, with other Al-rich phosphates; and (2) massive associations of multiple dark-colored Fe-Mn-rich phosphates dominated by lithiophilite-triphyllite.

In situ niobium and tantalum oxide minerals (NTO) have only been observed in the first group of Al-rich phosphatic nodules and in the albitized intermediate zones of the dike (Prado Araujo et al., 2023). The phosphatic nodules are characterized by both Nb-Ta-Fe-bearing rutile and columbite group minerals (CGM), while the albitized intermediate zones show only CGM. Ore mineral concentrates from Buranga are dominated by CGM, with traces of microlite, tapiolite, cassiterite, rutile, wodginite, and ixiolite (Melcher et al., 2015). Recent studies of the rare-metal mineralization

in the Gitarama-Gatumba field point to multi-stage processes, with at least three generations of cassiterite formed from a water-saturated melt system, with cassiterite precipitation triggered initially by local disequilibrium around the fast-growing pegmatitic minerals and later by metasomatic fluid-rock interactions (Hulsbosch and Muchez, 2020). Additionally, paragenesis of NTO in Buranga is divided into two phases with an early crystallization of rutile in the magmatic stage, and CGM precipitation at the magmatic-hydrothermal stage (Prado Araujo et al., 2023).

3. MATERIALS AND METHODS

The Python scripts used for all the data processing and graph plotting, along with the data from this study, are available in a dedicated online repository (https://github.com/thembubbles/Buranga_magmatic-hydrothermal_transition).

3.1. *Materials and sample location*

The samples used in this study are from the Buranga pegmatite, located in the Gitarama-Gatumba pegmatite field of Western Rwanda (Dewaele et al., 2011; Muchez et al., 2014; Hulsbosch et al., 2014). Phosphate minerals occur in polymineralic nodules up to tens of centimeters in size or larger. These phosphatic nodules occur incorporated in the quartz core zone and along the core margins within the Buranga dike (Polinard, 1950; Varlamoff, 1961; Fransolet, 1975; Dewaele et al., 2011). The crystallization of primary phosphates in these nodules is suggested to occur mostly after the crystallization of microcline and muscovite in the intermediate zone, but before the albitization stage (Fransolet, 1975).

The samples were retrieved from the Royal Museum for Central Africa mineral and rock collection and from the University of Liège collection. Samples were prepared into doubly polished thick wafers (150-300 μm) and examined under transmitted light on an Olympus BX40 petrographic microscope at the Department of Earth and Environmental Sciences of KU Leuven (Belgium) to search for fluid inclusion assemblages (FIA) and to determine their typologies and relations with the host phases. Additionally, to better understand the textural features in the host minerals, samples were coated with a ~20 nm layer of carbon and imaged by backscattered electrons (BSE) under an

acceleration voltage of 15 kV and beam current of 1 nA using a JEOL JXA-8530F field emission gun electron probe micro-analyzer (FEG-EPMA) at the Department of Materials Engineering, KU Leuven, Belgium. The same wafers were analyzed by all methods described below in this section.

3.2. *Fluid inclusion petrography*

The study of fluid inclusions in the phosphate minerals focused on primary fluid inclusion assemblages. Primary character was defined by inclusions distant from visible fractures and either occurring as random three-dimensional clusters, isolated position away from other inclusions, relatively large inclusions, or rarely following growth zones in the host mineral (Roedder, 1984; Van Den Kerkhof and Hein, 2001). The volume fraction of the carbonic vapor phase (fill rate) was estimated using the volumetric chart of Roedder (1984).

Fluid inclusion types are defined based on petrographic and microthermometric data. Fluid inclusions are classified into four types depending on the number of phases present at room temperature and the volumetric proportions between these phases. This classification is presented in more detail in section 4.2.

3.3. *Fluid inclusion microthermometry*

Microthermometry was conducted on a Linkam MDS600 heating and freezing stage coupled to an Olympus BX51 microscope at the Department of Earth and Environmental Sciences of KU Leuven. Stage calibration was done using phase transitions in the systems H_2O-CO_2, H_2O-NaCl, H_2O-KCl, and H_2O (i.e., Tm_{CO2}, Tm_{clath}, Th_{CO2}, Te_{NaCl}, Te_{KCl}, and Tm_{ice}) in synthetic fluid inclusions (SynFlinc, USA). The total homogenization temperature of pure H_2O (critical behavior at 374 ˚C) in the same synthetic fluid inclusions was applied as a reference for higher temperatures. Analysis accuracy is within ± 0.3 ˚C for temperatures measured between -70 ˚C and 32 ˚C and within ± 5 ˚C for temperatures above 32 ˚C.

The samples were first cooled to avoid stretching, leakage, and decrepitation of the fluid inclusions due to increased internal pressures during heating. Measured phase transitions include the temperature of first melting (T_{fm}), corresponding to the first visible appearance of a liquid from the solidified aqueous phase, melting of the carbonic phase (Tm_{CO2}), corresponding to the final melting

of the carbonic phase inside the frozen bubble, final melting of hydrohalite (Tm_{hh}), final melting of ice (Tm_{ice}), dissociation of clathrate (Tm_{clath}), and homogenization of carbonic phase (Th_{CO2}). The total homogenization temperature (Th_{tot}) of the fluid inclusions is only partially reported because most inclusions decrepitated before total homogenization. Phase transition temperatures were determined by cooling the inclusions to -190 ˚C and heating up to +32 ˚C. The heating rate varied from 10 to 30˚C/min depending on the proximity to the phase transitions but was reduced to 1˚C/min around these transitions. A cyclic heating-cooling procedure was carried out around the main phase transitions to improve measurement precision and avoid metastability effects (cf. CO_2 or Li-containing fluid inclusions, Diamond, 2001; Dubois et al., 2010). The total homogenization temperature was determined under atmospheric pressure by using a stepwise heating procedure, where inclusions were repeatedly assessed at 10 ˚C intervals. A heating rate of 40˚C/min was used from room temperature up to 200 ˚C and reduced to 5 ˚C/min from 200 ˚C to total homogenization or until 400 ˚C, when the experiments were stopped since most unhomogenized inclusions decrepitated. Details of the microthermometric procedures used can be found in Hulsbosch and Muchez (2020).

Fluid inclusions in phosphate minerals from Buranga were determined to be part of the H_2O-NaCl-KCl-LiCl-CO_2-N_2 system (see results section for further details). Currently, there is no direct thermodynamic model to calculate salinities for this system. Consequently, data processing followed the indirect salinity determination workflow: (1) the total salinity in $NaCl_{eq}$ mass% in the H_2O-NaCl-CO_2 system was calculated from the clathrate dissociation temperature (Tm_{clath}) by applying the equation from Darling (1991); (2) the partial salinities of each salt species were calculated from their molar concentration, obtained by LA-ICPMS analysis.

3.4. *Raman microscopy*

3.4.1. Instrumentation and data acquisition

Raman spectra were obtained at the Department of Chemistry of KU Leuven using a Horiba Jobin-Yvon LabRAM HR Evolution spectrometer coupled to an Olympus BX41 confocal microscope. Fluid inclusion phases (liquid, vapor, and solids) were excited with a Nd:YAG 532 nm

wavelength laser (Oxxius, 100 mW power). In cases where the host mineral showed strong photoluminescence, a He-Ne 633 nm wavelength laser (LASOS, 17 mW power) was used instead. The scattered light signal was measured with a Peltier-cooled Synapse (EM)-CCD detector. The reader is referred to Prado Araujo et al. (2021) for more details on the Raman instrumentation, methodology, and calibration procedures used in this study. The identification of mineral phases (both as hosts of fluid inclusions and solids inside them) is done primarily by Raman spectroscopy, assisted by transmitted-light petrography and BSE-EDS analyses.

Point measurements used a 100x microscope objective (Olympus, MPLN, NA 0.9). A single spectral window of 100 to 4000 cm^{-1} was selected in combination with a 150 grooves/mm grating, and a confocal pinhole aperture of 30 to 50 μm. The integration time of single analyses was from 40 s to 20 s depending on the size of the confocal pinhole. Raman maps were acquired using a 50x long-working distance objective (Olympus, LMPLFLN, NA 0.5) in a line-scan mapping array using the Horiba SWIFT® technology. Mapping settings intended to maximize the signal quality and area coverage while minimizing the total mapping time. Considering that each Raman map covered different minerals and areas, the required settings also varied. Analytical conditions varied from 0.2 s to 0.5 s single accumulations, arranged in regularly spaced arrays (2x2 or 5x5 μm), electron-multiplying gain between 300-800, 633 nm or 532 nm lasers, 25% or 100% laser power filter, 30-100 μm confocal pinhole, 150 grooves/mm grating with a range from 100 to 4000 cm^{-1}. The specific analytical settings for each map can be found in their respective legends. All measurements were acquired and treated with the LabSpec 6.5.2 software. Spectrometer X-axis calibration (Raman shift) was performed using the NIST-certified Horiba SP-RCO objective (polystyrene Raman peak at 1001.4 cm^{-1}). A spike filter was automatically applied during the analysis. Point analyses were subjected to subtraction of a 6-degree polynomial baseline correction with 50 attaching points. In the mapping datasets, processing steps included a 6-degree polynomial baseline subtraction with 150 attaching points, and a range reduction retaining only data between 400 and 3650 cm^{-1}. All Raman images in this manuscript were smoothed to improve the visualization of mineral contacts and to remove rastering effects.

3.4.2. *Calculation of molar fractions based on Raman spectroscopic measurements*

The calculation of gas species' molar fractions from Raman analysis of homogenized carbonic phases in fluid inclusions followed the procedure described by Burke (2001) using a slightly modified formula: $X_a = \frac{\left(\frac{A_a}{\sigma_a}\right)}{\sum_{i=a}^{n}\left(\frac{A_i}{\sigma_i}\right)}$. Where X_a, A_a, and σ_a are respectively the molar fraction, the Raman peak area, and the Raman cross-section for gas species a; while the lower term $\sum_{i=a}^{n}\left(\frac{A_i}{\sigma_i}\right)$ represents the sum of the ratios (peak area over cross-section) of each gaseous species present in the inclusion.

The instrumental efficiency is calibrated over the whole spectral range with an intensity correction curve, based on the irradiance spectrum of a NIST-certified Avantes AvaLight-HAL-CAL-Mini white light source. The calculation of peak areas was done separately for each peak using a local baseline fitting, and the Raman cross-sections used for CO_2 ν1, CO_2 2ν2, N_2, and CH_4 were calculated using the relative normalized differential Raman scattering cross-sections values (Σ) and the formula provided by Burke (2001).

3.5. *Laser ablation inductively coupled mass spectrometry (LA-ICPMS)*

Trace element compositions of individual fluid inclusions and their host minerals were measured with an Agilent 7900 Quadrupole ICP-MS, equipped with a collision-reaction cell at the GeoRessources Laboratory (Université de Lorraine, Nancy, France). Samples were ablated with an ESI New Wave Research UC 193 nm excimer laser. Analytes were carried by a He medium with a constant mass flow rate of 650 ml/min, which was then mixed with Ar (850 ml/min) before entering the ICP torch. 22 isotopes (^{7}Li, ^{11}B, ^{23}Na, ^{24}Mg, ^{27}Al, ^{29}Si, ^{31}P, ^{39}K, ^{43}Ca, ^{44}Ca, ^{47}Ti, ^{55}Mn, ^{56}Fe, ^{57}Fe, ^{85}Rb, ^{88}Sr, ^{93}Nb, ^{118}Sn, ^{133}Cs, ^{137}Ba, ^{181}Ta and ^{182}W) were measured concomitantly. The dwell time on each isotope was 0.02s, except for ^{23}Na, ^{29}Si, and ^{31}P, which were measured in 0.01s, and ^{93}Nb, ^{118}Sn, and ^{181}Ta, measured in 0.03s. Analyses were performed with two sets of conditions, depending on the host mineral. The first set, used for analyzing fluid inclusions in wyllieite, augelite and quartz, had a fluence of 5 J/cm^3, laser repetition rate of 5 Hz, and laser spot size of 20 μm. The second set, used in trolleite, bertossaite and brazilianite, had a fluence of 12 J/cm^3, laser repetition rate of 10 Hz, and laser spot size of 30 μm. In a few cases, where the inclusion size was larger than the laser spot,

297 the spot size was increased to cover the whole inclusion. The NIST 610 and 612 reference glasses
298 were used as external standards and were analyzed before, between, and after the unknowns with the
299 same acquisition settings (bracketing standardization procedure). The reference glass NIST 614 was
300 used to validate the analytical protocol, in particular accuracy and precision. The measured signal
301 was reduced in the SILLS software (Guillong et al., 2008) using the ^{23}Na concentration as internal
302 standard, as the total salinity (mass% $NaCl_{eq}$) obtained with the microthermometry, and applying the
303 charge-balance method (Allan et al., 2005) to correct for the presence of other relevant salts (i.e., Li,
304 Na, K, Rb, and Cs). The signal of fluid inclusions hosted in phosphates and quartz have been matrix-
305 corrected based on the stoichiometric Al_2O_3 or SiO_2 content of the host, respectively. Limits of
306 detection (LOD) and limit of quantification (minimum detectable value) were calculated following
307 the method of Pettke et al. (2012). Concentrations below the limit of quantification (around 6 times
308 the background counts) were rejected.

309 ## 4. RESULTS

310 ### 4.1. *Phosphate mineral sequences*

311 Phosphate minerals in the Buranga pegmatite occur as polymineralic nodules, commonly
312 showing complex textural relationships. Two types of associations are present in such nodules,
313 composed of either Fe-Mn-rich phosphates or Al-rich phosphates. This study focuses only on the Al-
314 rich phosphatic nodules, which also host part of the Nb-Ta mineralization in the Buranga dike (Prado
315 Araujo et al., 2023). Based on textural relations between the phosphate minerals (Prado Araujo et al.,
316 2023), a paragenetic sequence is observed in the Al-rich phosphatic nodules (Figure 1) and three main
317 crystallization stages are defined (Table 1).

318 Primary minerals occur as coarse- to fine-grained crystals (>2 cm to <1 mm) and are usually
319 anhedral to subhedral due to resorption and replacement by later phases, or occasionally euhedral
320 when occurring as inclusions (Figure 2A, B). Texturally, these minerals are in equilibrium with the
321 early medium, while in disequilibrium with the late medium. Wyllieite, F-rich montebrasite,
322 rosemaryite, trolleite, and quartz are defined as primary minerals (Prado Araujo et al., 2023). These
323 minerals are mostly devoid of primary fluid inclusions, with exception of trolleite and quartz, which

show many fluid inclusions, sometimes displaying multiple densely populated fields in the same crystal. However, early quartz crystals, preserved as inclusions in magmatic phosphates, can be barren of primary fluid inclusions (Figure 2A).

Early secondary minerals range from coarse- to very fine-grained (>2 cm to > 0.1 mm) crystals and are often subhedral to anhedral. They commonly occur enclosing anhedral crystals of the magmatic phases (Figure 2C, D), but also form interstitial crystals (Figure 2E, F). Early secondary minerals seem to precipitate from a medium that is in disequilibrium with the primary phases, but they are also texturally in disequilibrium with the latest lower-temperature medium. Replacement textures regularly appear as rounding of early phases due to partial dissolution, and precipitation of new phases around these resorbed crystals (Figure 2D, E, F). Bertossaite, F-poor montebrasite, scorzalite, augelite, and brazilianite are representatives of early secondary phases. Most of the quartz grains observed in the Buranga dike occur in paragenesis with these phosphates and, consequently, quartz is included at this stage. All these minerals show widespread occurrence of fluid inclusions, which in some cases (especially for montebrasite) makes it quite hard to unambiguously identify primary inclusions.

Late secondary minerals replace all earlier phases, mostly in fractures or cleavage planes and pseudomorphs after the original minerals. They dominantly occur as fine- to very fine-grained (< 1 mm) aggregates of euhedral to subhedral crystals and show complex replacement textures even within the group itself. They seem to precipitate from the latest medium, which is in disequilibrium with all the prior minerals. Eosphorite, samuelsonite, burangaite, wardite, and hydroxylapatite are highlighted from this group.

Table 1: Mineral stages and their respective phases observed in the Al-rich phosphatic nodules from the Buranga dike.

Primary	
Wyllieite	$NaNaMn(Fe^{2+}Al)(PO_4)_3$
F-rich montebrasite	$LiAl(PO_4)(OH,F)$
Rosemaryite	$\square NaMn^{2+}(Fe^{3+}Al)(PO_4)_3$
Trolleite	$Al_4(PO_4)_3(OH)_3$
Quartz	SiO_2
Early secondary	
Bertossaite	$Li_2CaAl_4(PO_4)_4(OH)_4$
F-poor montebrasite	$LiAl(PO_4)(OH)$
Scorzalite	$(Fe,Mg)^{2+}Al_2(PO_4)_2(OH)_2$
Augelite	$Al_2(PO_4)(OH)_3$
Brazilianite	$NaAl_3(PO_4)_2(OH)_4$
Quartz	SiO_2
Late secondary	
Eosphorite	$Mn^{2+}Al(PO_4)(OH)_2 \cdot H_2O$
Samuelsonite	$Ca_9Mn^{2+}{}_4Al_2(PO_4)_{10}(OH)_2$
Burangaite	$NaFe^{2+}Al_5(PO_4)_4(OH)_6.2H_2O$
Wardite	$NaAl_3(PO_4)_2(OH)_4.2H_2O$
Hydroxylapatite	$Ca_5(PO_4)_3(OH)$

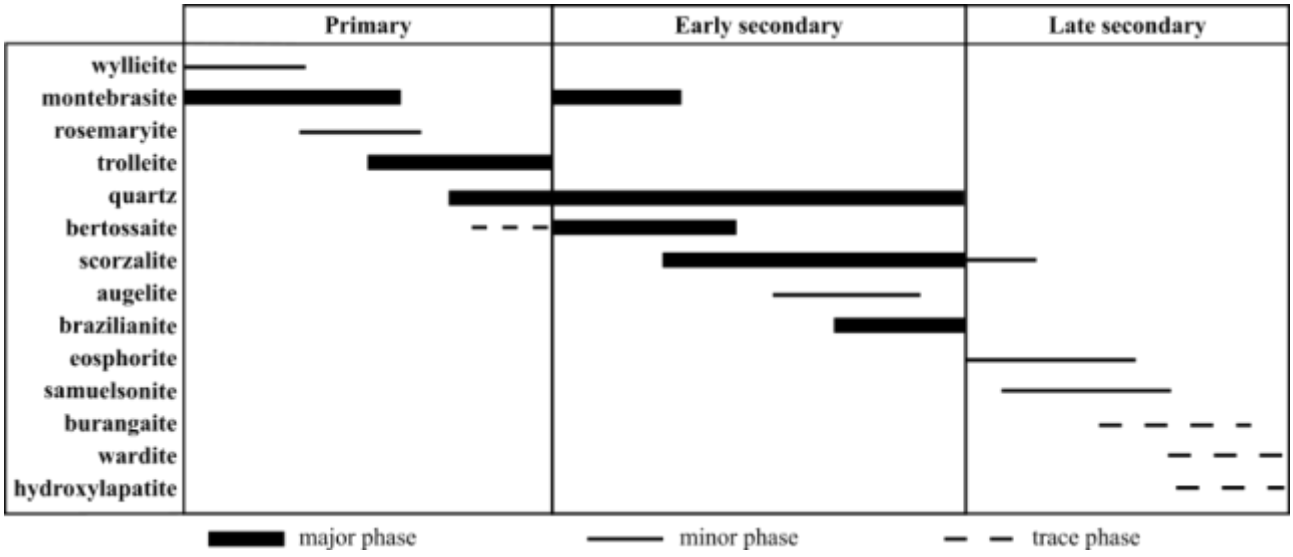


Figure 1: Paragenetic sequence of phosphate minerals in the Al-rich phosphatic nodules from the Buranga pegmatite.

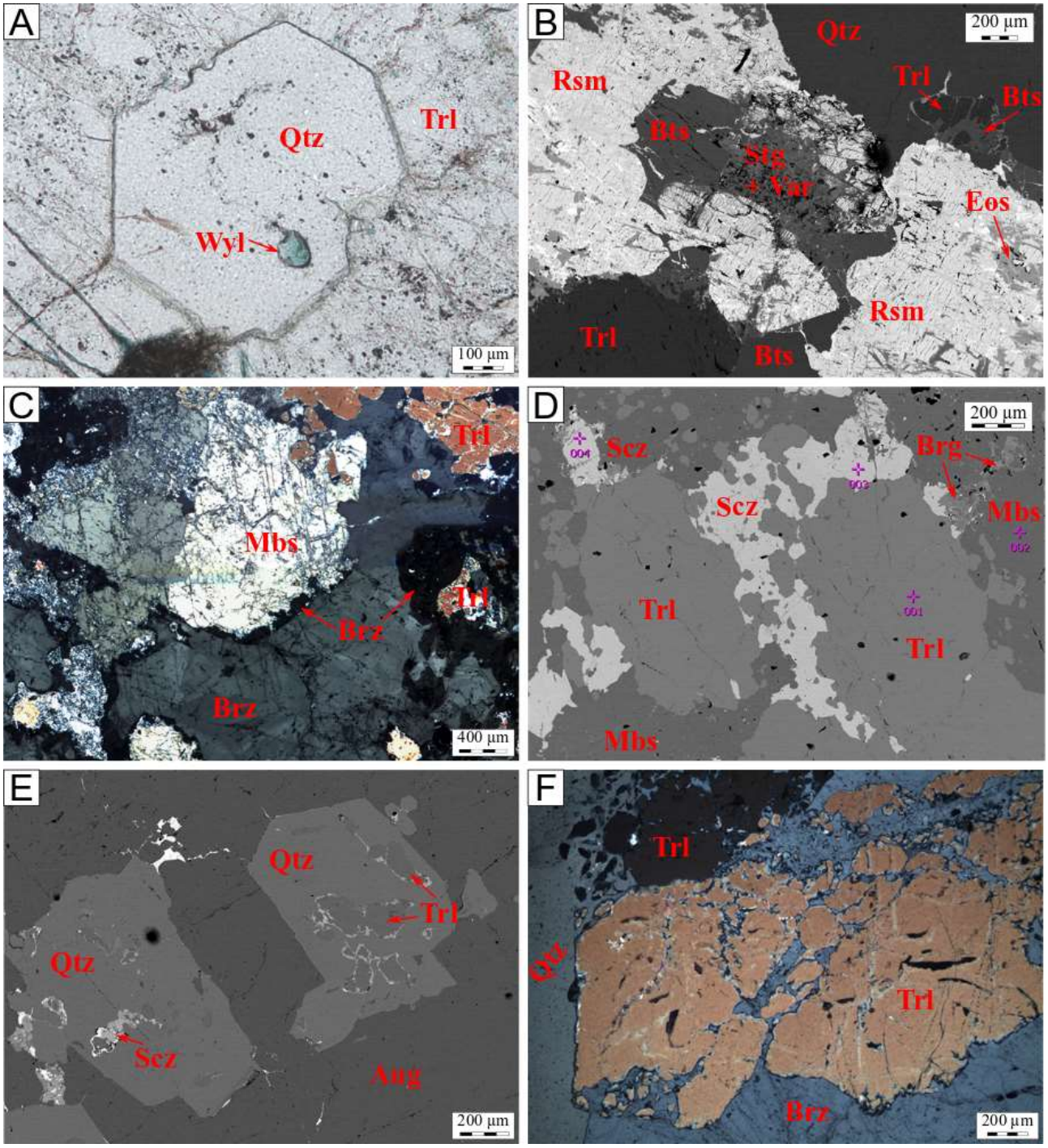


Figure 2: Photomicrographs of textures in the Al-rich phosphatic nodules from the Buranga pegmatite. **(A)** Anhedral wyllieite inclusion in euhedral quartz, which in turn is included in trolleite. Transmitted light image, plane polarizers. **(B)** Subhedral coarse-grained rosemaryite crystal surrounded by trolleite and quartz, and partially altered to eosphorite and strengite + variscite. Bertossaite is interstitial in relation to rosemaryite, but can be seen partially replacing trolleite on the top right of the image. Backscattered electron image. **(C)** Anhedral trolleite and subhedral montebrasite with interstitial brazilianite. Brazilianite also appears partially replacing both former phases (darker bands at crystal rims). Transmitted light image, crossed polarizers. **(D)** Anhedral trolleite grain partially replaced by scorzalite and surrounded by montebrasite. The scorzalite in turn is altered to burangaite and wardite. Backscattered electron image. **(E)** Anhedral trolleite restites rimmed by scorzalite and included in euhedral quartz, which in turn is surrounded by augelite. Backscattered electron image. **(F)** Anhedral trolleite fractured and surrounded by brazilianite and quartz. Transmitted light image, crossed polarizers. Mineral abbreviations: Aug = augelite, Bts = bertossaite, Brg = burangaite, Brz = brazilianite, Eos = eosphorite, Mbs = montebrasite, Qtz = quartz, Rsm = rosemaryite, Scz = scorzalite, Stg = strengite, Trl = trolleite, Var = variscite, Wyl = wyllieite.

4.2. *Fluid inclusion petrography*

Since the focus of this contribution is to characterize the fluid phase present when the phosphate minerals were precipitating, this study aimed at primary fluid inclusion assemblages. Pseudosecondary inclusions can also represent a fluid phase that coexisted with the host crystal, but since there is textural evidence of phosphate minerals' resorption followed by precipitation of secondary phases (Prado Araujo et al., 2023), the relation between crystal growth and fluid entrapment can be partially adulterated in fluid inclusion trails. Therefore, to avoid any ambiguity, only inclusions distant from visible fractures, not in trails, and either occurring as random three-dimensional clusters, large inclusions isolated from other inclusions, or following growth zones in the host mineral, more rarely in this case, were analyzed.

Not all phosphate minerals show fluid inclusions that can be analyzed, either because they are too small (<5 μm), the exact temporal relation between host and inclusions (primary, pseudosecondary, or secondary) cannot be clearly defined, the host mineral is not transparent to the light source. Nevertheless, the main minerals in the magmatic-hydrothermal transition (Figure 3) are analyzed to reveal the fluid evolution during the crystallization of the Buranga dike.

Four petrographic types of fluid inclusions are observed in the samples of Buranga (Figure 4). These types are defined depending on the number of phases present at room temperature, the volumetric proportions between these phases, and their composition (Table 2). Type 1 inclusions are defined as presenting three or more phases at room temperature: an aqueous liquid, a carbonic vapor bubble, and one or more solids. Type 2A inclusions have two phases: an aqueous liquid and a carbonic vapor bubble occupying less than 30-35% of the inclusion volume. Type 2B inclusions also have two phases: an aqueous liquid and a carbonic vapor bubble, but in this case, the vapor occupies more than 50% of the inclusion volume. Type 3 inclusions have three phases present at room temperature: an aqueous liquid, a carbonic liquid, and a carbonic vapor bubble. Phosphate minerals in the Buranga dike commonly show more than one fluid inclusion type within the same assemblage, but the number and occurrence of such types is variable between the observed minerals.

4.2.1. Fluid inclusions in primary minerals

Wyllieite has only inclusions of type 1 (L-V-S), with small cubic to rounded colorless solids. Raman analyses of the solids indicate that they are rhodochrosite ($MnCO_3$). The volumetric proportion within inclusions is similar in all analyses, with a vapor fill rate of about 20% and solids occupying 2 to 4% of the whole inclusion. Trolleite shows almost all inclusion types, except for type 3 (L-L-V). All types occur together in the same field, but they are not distributed in equal numbers (Figure 5). Inclusions from type 2A (V-L) are by far more common, dominating all the observed fields, and are followed by type 1 (L-V-S). Type 2B (V-L) inclusions are mostly rare, occurring only as one or two inclusions in some fields. Type 1 (L-V-S) inclusions in trolleite show montebrasite ($LiAlPO_4OH$) as a solid phase (2 to 20% of inclusion volume). Additionally, some inclusions can show more than one crystalline phase (Figure 6), presenting a high proportion of solid phases (up to 70% of inclusion volume). These crystal-rich inclusions show variable proportions of montebrasite, burangaite ($NaFe^{2+}Al_5(PO_4)_4(OH)_6.2H_2O$), rutile ($TiO_2$), and more rarely, wardite ($NaAl_3(PO_4)_2(OH)_4.2H_2O$). In extreme cases, the crystal-rich inclusions do not contain any aqueous liquid, showing only solids and carbonic phases (Figure 6). The solid phases do not dissolve into the fluid phase while heating the inclusions (i.e., the volume and shape of solids remain constant during homogenization experiments, even after L-V homogenization, and do not change until inclusion decrepitation). Other magmatic minerals showing substantial fluid inclusion assemblages were scarce. Some primary phosphates are intensely replaced, obstructing a clear identification of primary fluid inclusions from the magmatic stage (e.g., F-rich montebrasite), whereas others were too dark and did not host visible fluid inclusions (e.g., rosemaryite).

4.2.2. Fluid inclusions in secondary minerals

Bertossaite shows mostly inclusions of type 2A (L-V), followed by type 3 (L-L-V). There are rare cases where a solid phase (identified as quartz by Raman spectroscopy) is observed in the inclusions (type 1 L-V-S). Scorzalite has only inclusions from type 2A (V-L) with a relatively constant fill rate (20-35%). Augelite most commonly shows type 2A (L-V) inclusions, with rare occurrences of type 1 (rutile is the solid observed in these inclusions), and type 2B. Brazilianite shows

inclusions from type 1 (quartz as solid inclusions), 2A, and 3 (Figure 4). Quartz only shows fluid inclusions of type 2A, but their fill rate is quite variable (10-40%). Additionally, some quartz samples show solid inclusions along with fluid inclusions. Although no fluid is observed in these solid inclusions, they may contain multiple crystalline phosphate phases inside (Figure 7), all of which are also observed in the phosphatic nodules.

Late secondary minerals, even though common, are generally small and no fluid inclusions could be observed in them.

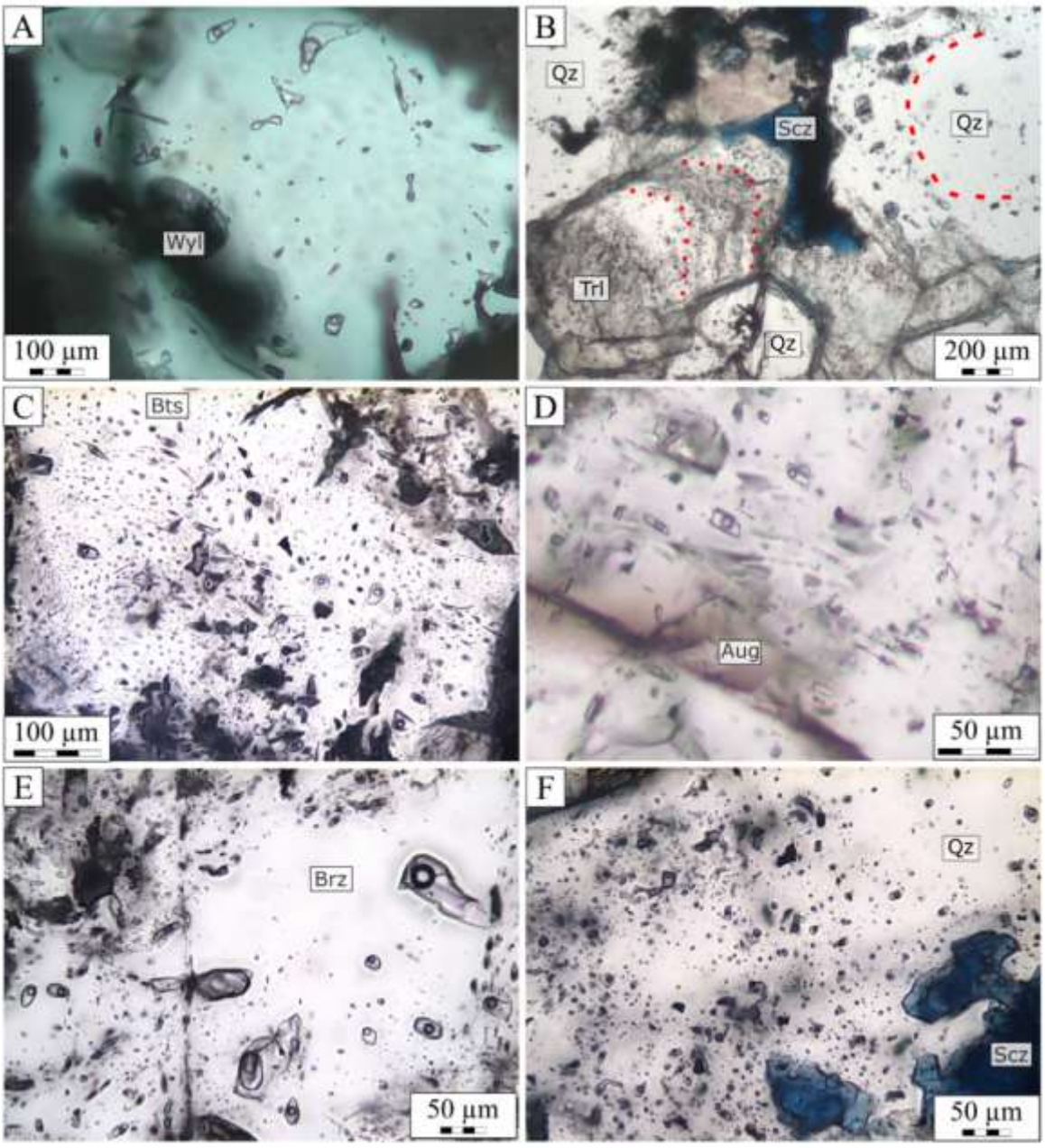


Figure 3: Transmitted light photomicrographs, transmitted light with parallel polarizers, of fluid inclusion fields in phosphates from Al-rich phosphatic nodules from the Buranga pegmatite. **(A)** Fluid inclusion assemblage (FIA) in wyllieite (Wyl). **(B)** Primary fluid inclusions following growth zones (dashed lines) in trolleite (Trl) and quartz (Qz). In this quartz crystal, fluid inclusions are also associated with mono- and multi-mineral solid inclusions. **(C)** FIA in bertossaite (Bts). **(D)** FIA in augelite (Aug). **(E)** FIA in brazilianite (Brz). **(F)** High density of fluid inclusions in quartz crystal (Qz) associated with scorzalite (Scz).

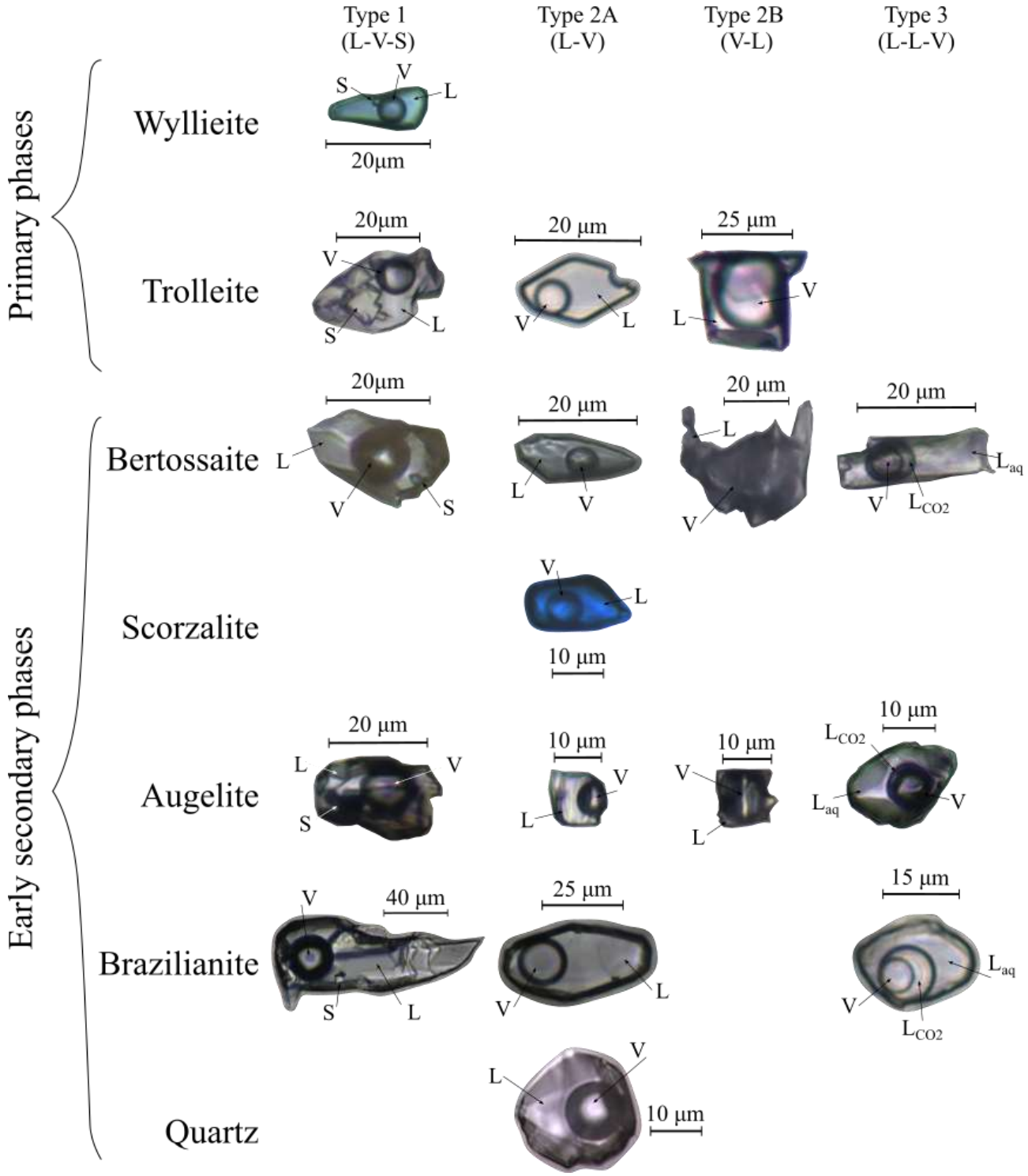


Figure 4: Petrographic classification of fluid inclusions in phosphate minerals from the Buranga pegmatite. Fluid inclusions are separated into petrographic types and related to the host phase.

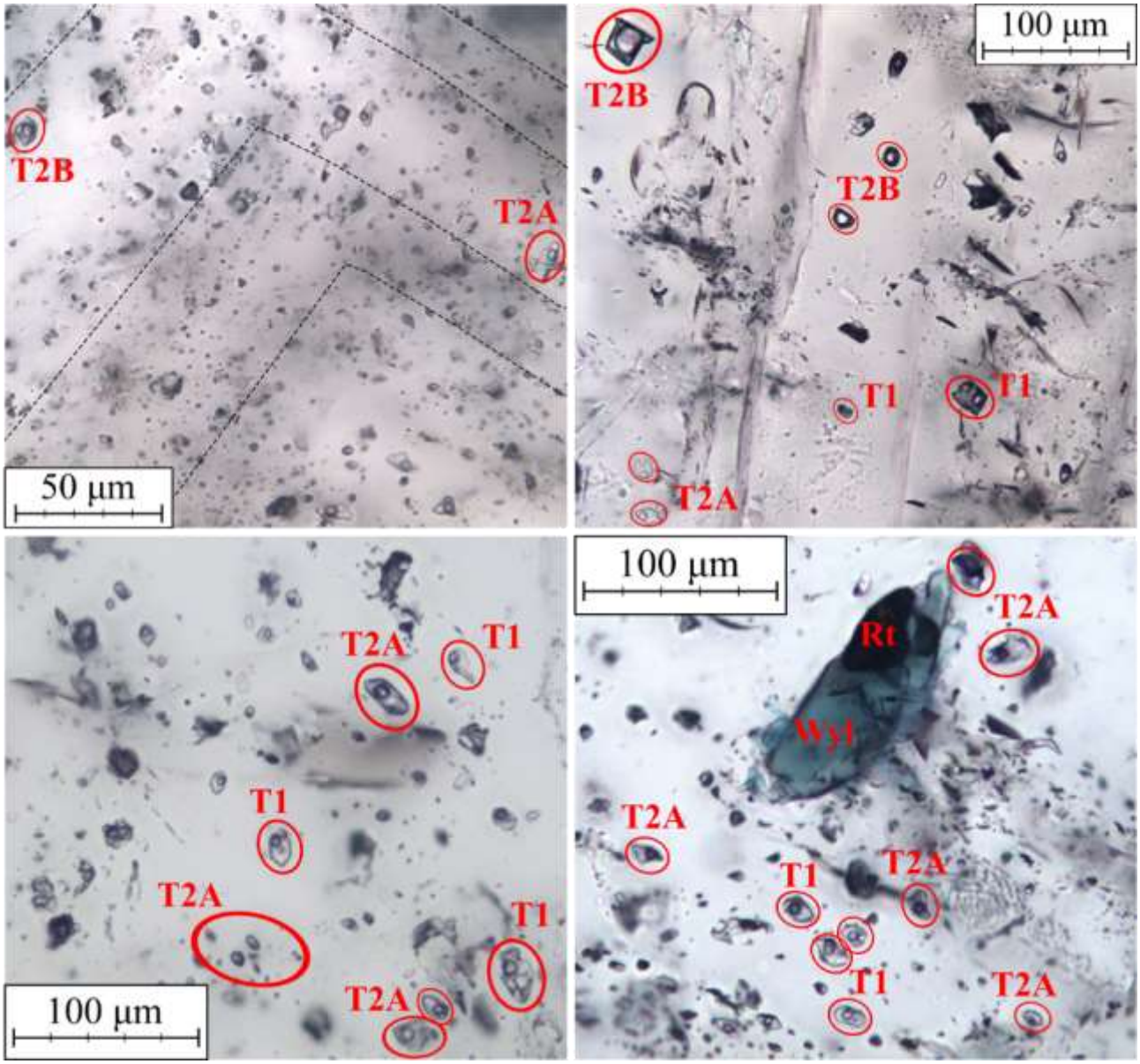
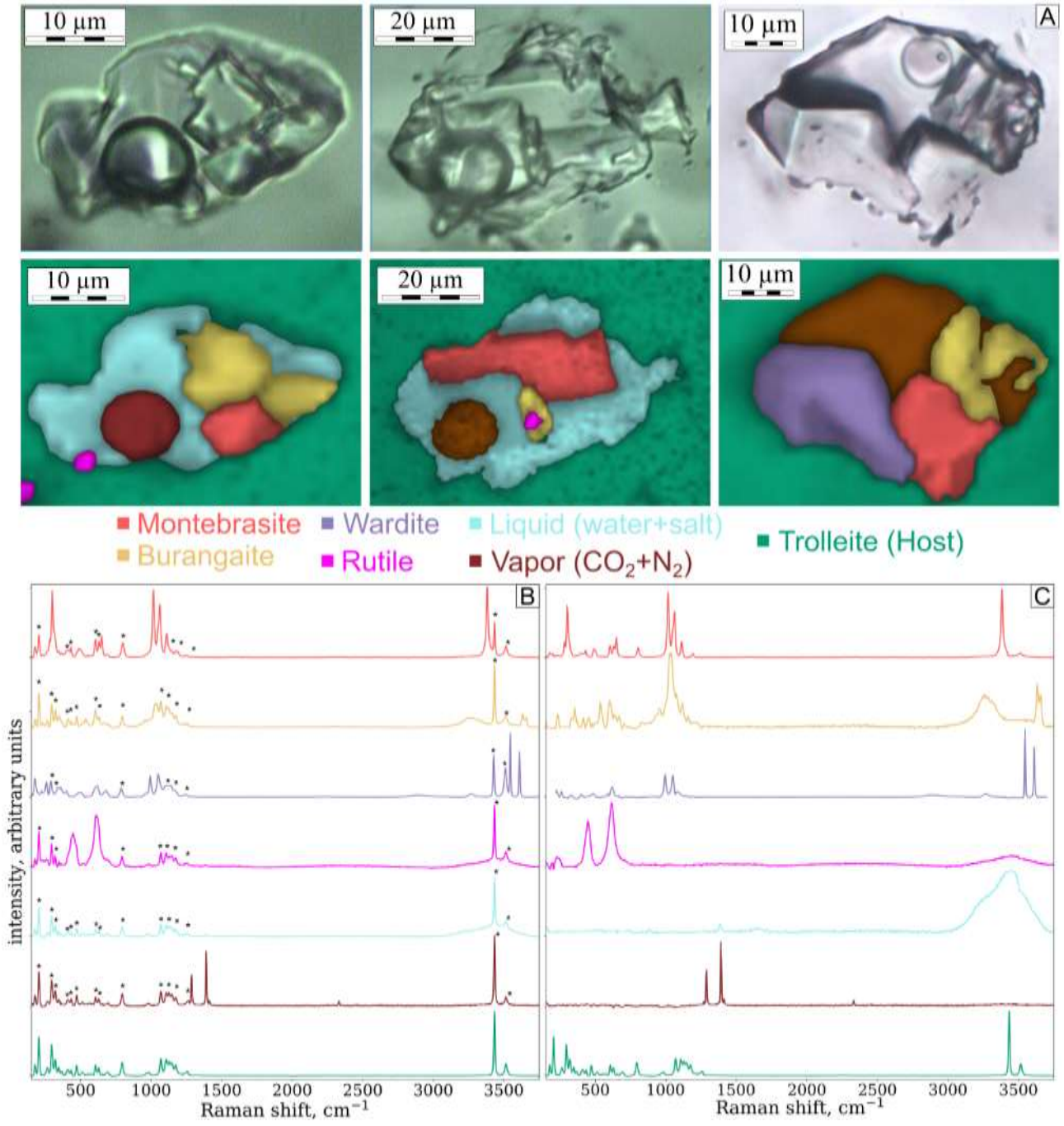


Figure 5: Photomicrographs of fluid inclusion fields in trolleite. The fluid inclusion types present in each field are highlighted (T1 = type 1; T2A = type 2A; T2B = type 2B). Rt = rutile and Wyl = wyllieite solid inclusions in trolleite.



447

448 **Figure 6:** Crystal-rich fluid inclusions in trolleite from the Al-rich phosphatic nodules from the Buranga pegmatite. **(A)**
449 Transmitted light photomicrographs and Raman phase maps of crystal-rich inclusions from different fields in trolleite. **(B)** Raman
450 spectra (baseline-corrected) of the observed phases. Asterisks represent peaks from the host phase (trolleite). **(C)** Processed Raman
451 spectra after removal of the host bands (subtraction of host spectrum from phase spectrum).

452

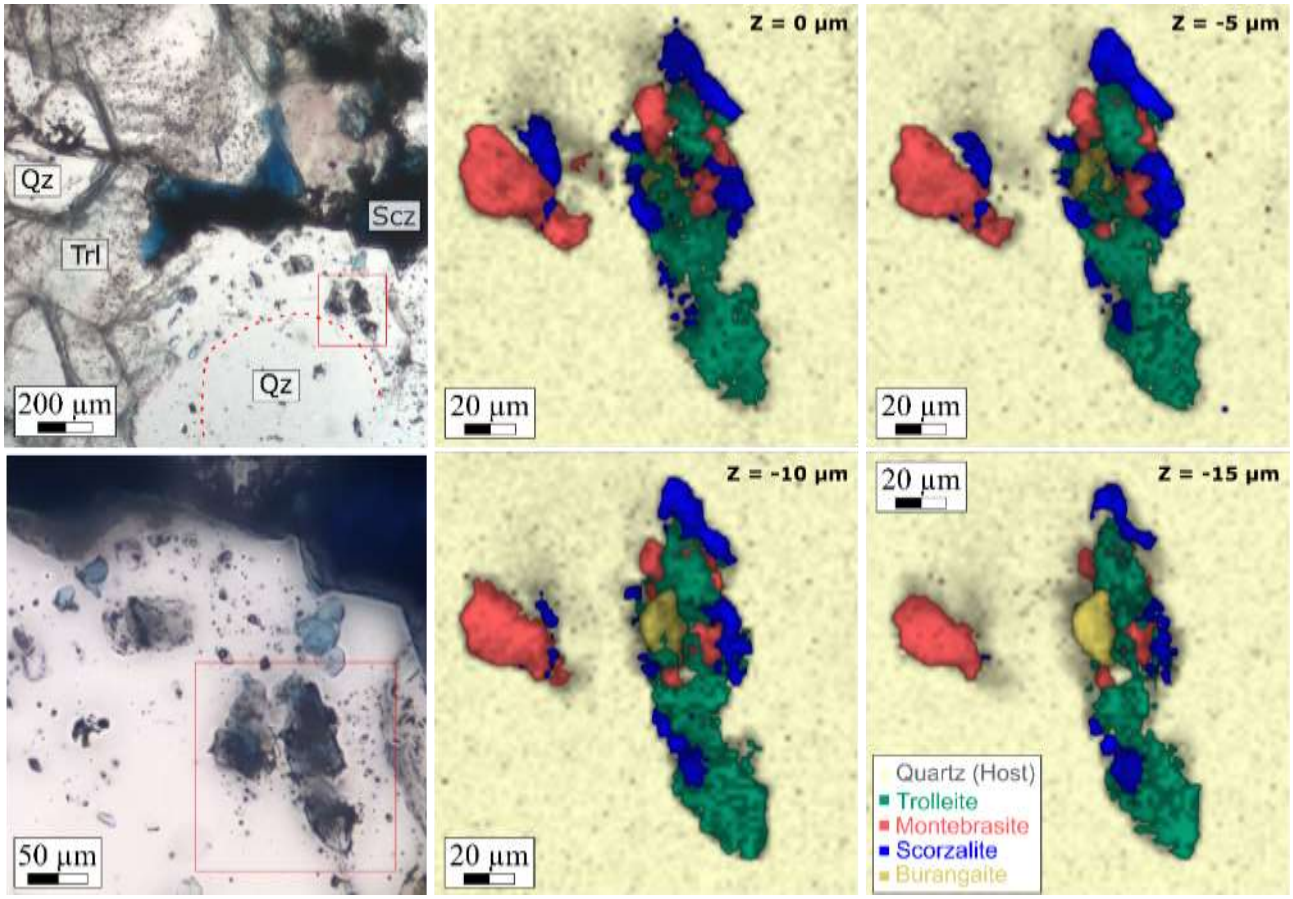


Figure 7: Transmitted light (left column) and Raman phase maps at multiple depths (middle and right columns) from a multi-phase solid inclusion (possibly a melt inclusion) in quartz. This is the same location represented in Figure 3B.

4.3. *Fluid properties*

4.3.1. Aqueous phase

In cooling-heating experiments, fluid inclusions mostly showed six phase transitions: final melting of the carbonic phase (Tm_{CO2}), first melting of the aqueous phase (Tfm), final melting of the salt hydrate phase (Tm_{hh}), final melting of ice (Tm_{ice}), final dissociation of the gas hydrate (Tm_{clath}), and homogenization of the carbonic phase (Th_{CO2}). The microthermometric values for fluid inclusions in phosphates minerals from the Buranga pegmatite are summarized in Table 2.

Although not always clearly observed, studied inclusions showed very low first melting temperatures, from -77 ˚C to -60 ˚C, with an average of -74 ˚C, corresponding to a mixture of NaCl and LiCl (± KCl) dissolved in the aqueous phase (Dubois et al., 2010). It is important to note here that these low first melting temperatures are only observed after cooling inclusions to -190 ˚C (Dubois et al., 2010; Hulsbosch and Muchez, 2020). When inclusions are cooled to -110 ˚C or higher

469 temperatures, no changes are observed until around -35 ˚C, which could be erroneously identified as
470 the first melting.

471 Hydrohalite is the only salt hydrate observed. It appears as tiny rounded prismatic crystals with
472 high relief relative to ice and is slightly blueish/greenish to colorless. Melting of hydrohalite was
473 between -29 ˚C and -18 ˚C for all minerals (Figure 8A), with the lowest averages associated with
474 brazilianite and quartz, regardless of the fluid inclusion type in these minerals. Final ice melting varies
475 from -24 ˚C to -3 ˚C (Figure 8B), with the lowest values associated with quartz and trolleite. The final
476 clathrate dissociation temperature ranges from -9 ˚C to +8 ˚C (Figure 8C).

477 In all cases when a solid phase is observed inside the inclusion at room temperature (type 1), the
478 solid volume does not change during heating (i.e., no dissolution of solids) until the inclusion
479 decrepitates, which commonly occurs before the total homogenization. The salinity of solid-bearing
480 inclusions (type 1) is calculated in the same way as inclusions from the other types, i.e. from the
481 dissociation temperature of clathrate as if no solid phase was present (section 3.3).

482 The fluid salinity varies between the crystallization stages, also varying among inclusion types
483 in the same mineral. Wyllieite and trolleite (primary phosphates) have salinities of 13.8 ± 0.1 and
484 13.0 ± 2.3 $NaCl_{eq}$ mass% (median ± standard deviation), respectively. Conversely, vapor-rich
485 inclusions (type 2B) in trolleite have lower salinities of 8.7 ± 2.5 $NaCl_{eq}$ mass%. Secondary
486 phosphates have a large distribution of the salinity values, with slightly higher values for bertossaite
487 type 3 (17.8 ± 2.8), quartz type 2A (15.9 ± 1.8), scorzalite type 2A (15.2 ± 2.9), augelite types 1, 2A
488 and 3 (14.6 ± 0.8), and brazilianite type 3 (14.5 ± 3.5). The lower values are represented by augelite
489 type 2B (13.1), bertossaite type 2A (11.5 ± 2.1), brazilianite type 2A (10.7 ± 1.8), bertossaite type 1
490 (9.4 ± 1.9), brazilianite type 1 (9.3 ± 1.8), and bertossaite type 2B (4.0).

491 Heating experiments do not show clear trends in total homogenization temperatures between the
492 phases studied (Table 2). Fluid inclusions present median T_h values around 320 ˚C and generally
493 homogenize to the liquid. Only inclusions in quartz have slightly higher T_h values than this median,
494 whereas it is lower for inclusions in brazilianite. However, unhomogenized fluid inclusions
495 commonly start to decrepitate at around 300 ˚C, with only few remaining intact up to T_h. Furthermore,

many fluid inclusions that did not decrepitate during heating and have been homogenized do not show the same properties (e.g., shape, vapor fill rate, color) compared to original inclusions before the experiments.

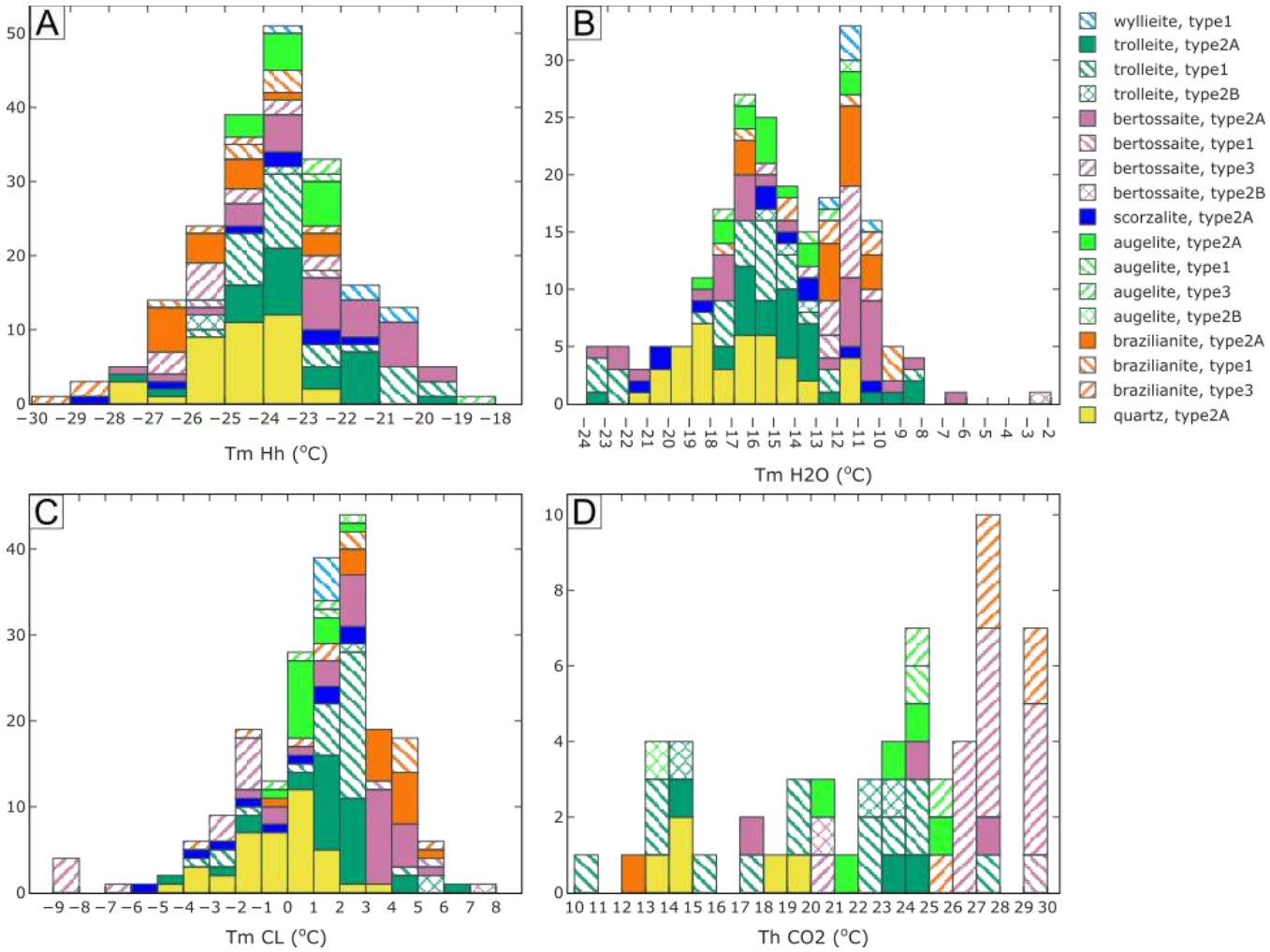


Figure 8: Histograms showing the data distribution of the microthermometric measurements for each fluid inclusion type observed in the phosphatic nodules from the Buranga pegmatite.

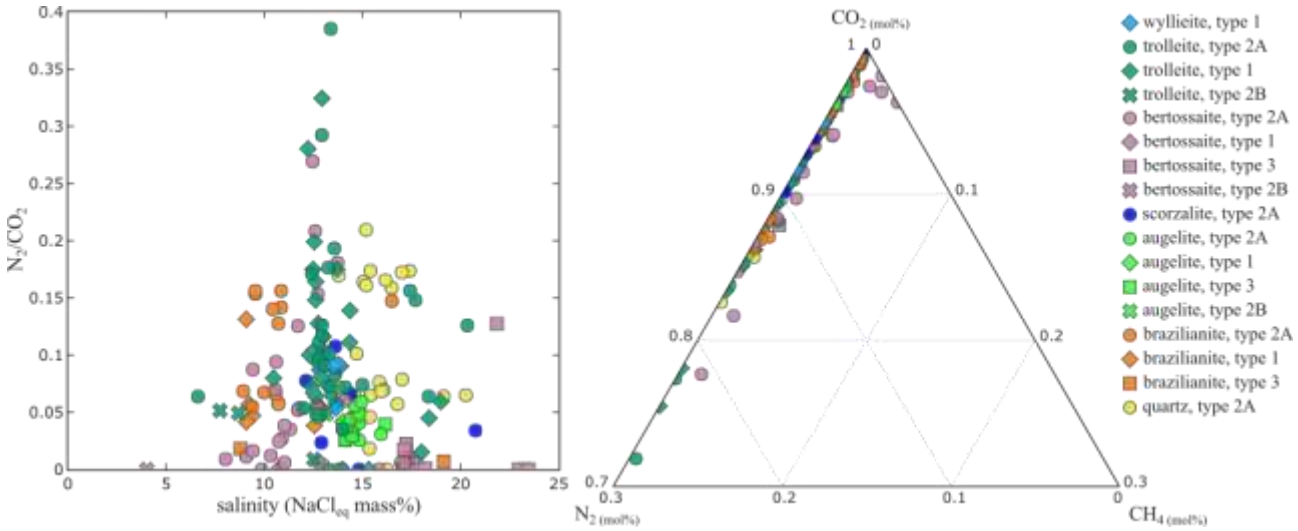


Figure 9: (A) Scatter plot of the N_2/CO_2 molar ratio (measured by Raman spectroscopy) versus salinity (calculated from the clathrate dissolution temperature obtained by microthermometry) of fluid inclusions in phosphate minerals from the Buranga pegmatite. **(B)** Ternary plot of the composition of the carbonic phase (mol%) measured by Raman spectroscopy of the homogenized carbonic phase. The color code references to the host mineral, while the symbols represent the fluid inclusion petrographic types.

Table 2: Petrographic and microthermometric data of fluid inclusions hosted in phosphate minerals from Al-rich phosphatic nodules from the Buranga pegmatite. Values are represented as median ± standard deviation. All inclusions are treated in the same geochemical system of NaCl-KCl-LiCl-H_2O-CO_2-N_2.

Stage	Mineral	Type	n	Size range (µm)	Phases at 25 ˚C	Carbonic filling (vol%)	Tm CO_2 (˚C)	Tm Hh (˚C)	Tm H_2O (˚C)	Tm Clath (˚C)	Th CO_2 (˚C)	Th total (˚C) [homog mode]	Salinity ($NaCl_{eq.}$%)
Primary	Wyllieite	Type 1	5	5-30	L-V-S	20 ± 1	n.o.	-21.4 ± 1.0	-11.1 ± 0.8	1.6 ± 0.1	n.o.	300 ± 1 [L]	13.8 ± 0.2
	Trolleite	Type 2A	31	5-50	L-V	25 ± 5	-56.9 ± 0.8	-23.5 ± 1.6	-14.8 ± 2.3	2.0 ± 2.2	n.o.	320 ± 30 [L]	13.3 ± 2.7
		Type 1	27	10-55	L-V-S	22 ± 4	-57.1 ± 0.7	-23.7 ± 1.7	-16.0 ± 3.7	2.2 ± 1.8	19.5 ± 5.4	320 ± 25 [L]	12.9 ± 2.0
		Type 1	6	15-30	S-L-V	12 ± 8	-57.4 ± 0.6	-21.7 ± 1.6	-16.0 ± 3.2	2.6 ± 1.2	21.1 ± 5.5	280 ± 35 [V]	12.4
		Type 2B	3	9-15	V-L	55 ± 5	-58.6 ± 1.2	-25.3 ± 1.0	-14.6 ± 0.9	5.2 ± 1.7	23.0 ± 5.3	n.o.	8.7 ± 2.5
Secondary	Bertossaite	Type 2A	31	5-70	L-V	21 ± 5	-56.8 ± 0.4	-22.2 ± 1.9	-12.3 ± 4.5	3.2 ± 1.7	24.1 ± 4.9	320 ± 20 [L>V]	11.7 ± 2.1
		Type 3	14	10-80	L-L-V	25 ± 3	-56.6 ± 1.5	-25.0 ± 1.4	-11.8 ± 1.1	-2.1 ± 3.2	27.4 ± 2.2	310 ± 30 [L]	17.8 ± 2.8
		Type 1	2	5-30	L-V-S	21 ± 10	-56.6	-24.2 ± 2.6	-12.1 ± 0.1	4.7 ± 1.3	29.1	n.o.	9.4 ± 1.9
		Type 2B	1	30	V-L	60	-57.5	n.o.	-2.6	7.9	20.4	n.o.	4.0
	Scorzalite	Type 2A	12	5-20	L-V	28 ± 5	-56.7 ± 0.7	-23.4 ± 2.2	-15.4 ± 3.7	0.3 ± 2.8	n.o.	n.o.	15.2 ± 2.9
	Augelite	Type 2A	14	5-20	L-V	20 ± 7	-57.0 ± 0.7	-23.2 ± 0.8	-15.7 ± 2.1	0.9 ± 0.6	23.6 ± 2.0	315 ± 15 [L]	14.6 ± 0.7
		Type 1	1	20	L-V-S	25	-56.6	-21.2	-14.0	1.4	24.1	n.o.	14.0
		Type 2B	1	10	V-L	60	-56.9	n.o.	-11.4	2.1	13.9	n.o.	13.1
		Type 3	3	5-50	L-L-V	25 ± 10	-57.8	-22.8 ± 2.6	-16.9 ± 2.5	1.0 ± 0.9	25.1 ± 0.6	n.o.	14.5 ± 1.1
	Brazilianite	Type 2A	18	10-40	L-V	23 ± 3	-57.2	-25.4 ± 1.6	-11.9 ± 2.1	3.9 ± 1.4	12.5	265 ± 25 [L]	10.7 ± 1.8
		Type 1	6	10- 50	L-V-S	22 ± 3	-57.2 ± 0.1	-24.0 ± 1.3	-10.7 ± 3.5	4.8 ± 1.3	n.o.	290 ± 10 [L]	9.3 ± 1.8

		Type 3	6	10-50	L-L-V	33 ± 10	-62.3 ± 0.7	-26.8 ± 2.8	-12.7 ± 1.7	1.0 ± 2.9	27.1 ± 1.6	n.o.	14.5 ± 3.5
	Quartz	Type 2A	43	5-30	L-V	25 ± 5	-57.4 ± 1.5	-24.1 ± 1.4	-1516.7 ± 3.0	-0.4 ± 2.0	14.3 ± 2.9	360 ± 25 [L]	16.0 ± 2.2

n = number of fluid inclusions analyzed; n.o. = not observed; homogenization mode: L = to liquid, V = to vapor

513

514 *4.3.2. Vapor composition*

515 When observed, melting of the carbonic phase was mostly lower than -56.6 ˚C (temperature for
516 the pure CO_2 system), except for some fluid inclusions in bertossaite, which show Tm_{CO2} close or at
517 -56.6 ˚C. Nevertheless, in many inclusions, phase transitions of the carbonic phase (Tm_{CO2}, Th_{CO2})
518 could not be observed, which is related to the low density of the gaseous components (Van Den
519 Kerkhof and Thiéry, 2001).

520 Raman spectroscopic measurements of the homogenized carbonic phase within inclusions (Table
521 3) show that these are mainly composed of CO_2 with variable but most often low amounts of N_2
522 (Figure 9B). In the primary minerals, N_2 varies from around 5 to 25 mol% (median at 8.3 mol%),
523 while it is lower than 10 mol% in the secondary minerals (median at 3.9 mol%), sometimes even
524 close to zero (e.g., vapor in most bertossaite inclusions is pure CO_2). For each mineral phase studied,
525 the lowest N_2 values are observed in type 3 inclusions (L-L-V), which also show a carbonic liquid.
526 CH_4 is rarely present, only in a few inclusions, and always below 2 mol% (Figure 9B).

527

528 **Table 3:** Composition of vapor bubble measured by Raman spectroscopy in fluid inclusions from the Al-rich phosphatic nodules.
529 Median values of mol % with standard deviations.

Stage	Mineral	Type	n	CO_2 (mol%)	N_2 (mol%)
Primary	Wyllieite	Type 1	5	92 ± 1	8 ± 1
	Trolleite	Type 1	29	91 ± 6	9 ± 6
		Type 2A	25	91 ± 6	9 ± 6
		Type 2B	5	95 ± 2	5 ± 2
Secondary	Bertossaite	Type 1	1	100 ± 0	0 ± 0
		Type 2A	29	96 ± 4	4 ± 4
		Type 2B	1	100 ± 0	0 ± 0
		Type 3	13	100 ± 3	0 ± 3
	Scorzalite	Type 2A	7	96 ± 3	4 ± 3
	Augelite	Type 1	1	96 ± 0	4 ± 0
		Type 2A	14	96 ± 1	4 ± 1
		Type 2B	1	95 ± 0	5 ± 0
		Type 3	3	97 ± 1	3 ± 1
	Brazilianite	Type 1	6	95 ± 3	5 ± 3
		Type 2A	17	94 ± 4	6 ± 4
		Type 3	6	97 ± 2	3 ± 2
	Quartz	Type 2A	37	94 ± 5	6 ± 5

530

4.4. *Bulk chemical composition*

LA-ICPMS analyses of fluid inclusions in all minerals show a dominant alkali metal content (mainly Na and K, with some Li, Rb, and Cs). The total alkali content in fluid inclusions mostly varies from 2.5 ± 1.4 (median ± σ) and 6.1 ± 1.1 mass% in the primary phosphates (wyllieite and trolleite, respectively) to 4.1 ± 2.0, 6.7 ± 0.5, and 4.4 ± 0.9 mass% in the secondary phosphates (bertossaite, augelite, and brazilianite, respectively). Fluid inclusions in quartz have a total alkali content of 5.6 ± 2.8 mass%. It is worth noting that vapor-rich inclusions (type 2B), although rare, show lower alkali contents when compared to other types in the same host (Table 4).

Na is the major cation in most fluid inclusions,. Only some inclusions in trolleite and, less markedly, in augelite show higher K concentration. Bertossaite shows relatively high amounts of Li (Figure 10A and Figure 11). Regarding the alkali element ratios (Figure 10B), wyllieite and bertossaite show higher Na/K and lower Na/Li ratios than the other minerals, whereas brazilianite appears with intermediate values between the K-rich (trolleite, augelite, and quartz) and the Li-rich (wyllieite and bertossaite) groups. Mn and Fe are present in most fluid inclusions (below 5000 ppm). B is also commonly observed in most inclusions with higher values in trolleite, augelite, and brazilianite, but its content is highly variable between the many minerals, varying from 100 to 3300 ppm. The same behavior is observed for Mg, with values ranging between 10 and 3000 ppm. Ca is below the detection limit in most fluid inclusions, being observed only in fluid inclusions in bertossaite and rarely brazilianite. HFSE (Ti, Nb, Ta, W) and Sn are present in low concentrations (10s to 100s of ppm) and do not show any correlation with the different crystallization phases. The other elements analyzed are either regularly below the detection limit (Ba and Sr) or show problems in the data reduction due to high concentrations in the matrix (Al, P, and Si).

553 **Table 4:** LA-ICPMS data of fluid inclusions in the Al-rich phosphatic nodules from the Buranga pegmatite. Values are in ppm, except for the total alkali content, which is in mass%.

Stage	Mineral	Type		Li	B	Na	Mg	K	Ca	Ti	Mn	Fe	Rb	Nb	Sn	Cs	Ta	Alkalis (%)
Primary	Wyllieite	Type 1	Nr	7	5	7	4	7	1	1	5	6	6	2	1	6	0	7
			Median (σ)	584 (683)	286 (256)	22900 (14143)	261 (268)	2025 (2134)	338 (0)	5.0 (0)	10171 (9545)	22807 (5594)	112 (106)	0.82 (0.05)	0.33 (0)	42 (38)	b.d.l.	2.5 (1.4)
	Trolleite	Type 1	Nr	13	9	15	8	15	0	5	11	7	15	6	5	14	6	15
			Median (σ)	973 (774)	1211 (541)	29473 (7934)	275 (464)	30731 (8563)	b.d.l.	94 (657)	378 (2637)	2309 (13760)	1151 (508)	4.3 (5.3)	293 (189)	406 (294)	35 (57)	6.3 (0.64)
		Type 2A	Nr	10	6	11	7	11	0	1	9	3	11	3	2	11	3	11
			Median (σ)	758 (1893)	1310 (926)	33322 (10230)	95 (894)	27345 (12382)	b.d.l.	298 (0)	617 (463)	1704 (670)	992 (430)	14 (9.7)	281 (222)	300 (231)	12.9 (17.5)	6.1 (1.2)
		Type 2B	Nr	2	1	3	3	3	1	0	2	3	2	0	1	2	2	3
			Median (σ)	730 (283)	1431 (0)	22167 (6871)	195 (2705)	21111 (8505)	52707 (0)	b.d.l.	1168 (1052)	3982 (2074)	1040 (737)	b.d.l.	112 (0)	489 (5.0)	19 (15.2)	4.3 (1.5)
Secondary	Bertossaite	Type 1	Nr	0	0	1	1	1	0	0	0	0	1	0	0	1	0	1
			Median (σ)	b.d.l.	b.d.l.	41452 (0)	17 (0)	2812 (0)	b.d.l.	b.d.l.	b.d.l.	b.d.l.	332 (0)	b.d.l.	b.d.l.	267 (0)	b.d.l.	4.5 (0)
		Type 2A	Nr	19	23	27	15	26	14	10	20	18	27	5	1	25	7	27
			Median (σ)	2375 (1895)	751 (306)	20913 (9932)	52 (109)	8180 (5917)	9626 (7921)	68 (127)	928 (1290)	1408 (3574)	340 (254)	0.39 (0.27)	7.9 (0)	59 (94)	4.1 (4.0)	3.5 (1.3)
		Type 2B	Nr	1	2	2	0	2	1	0	1	1	2	0	0	2	0	2
			Median (σ)	2281 (0)	289 (202)	6494 (5637)	b.d.l.	3063 (3626)	4098 (0)	b.d.l.	155 (0)	1873 (0)	190 (243)	b.d.l.	b.d.l.	42 (43)	b.d.l.	1.1 (0.79)
		Type 3	Nr	7	8	9	6	9	6	1	8	7	9	0	0	9	0	9
			Median (σ)	7156 (2305)	389 (107)	37009 (16562)	80 (180)	12770 (7938)	9017 (6811)	281 (0)	1405 (613)	2197 (4164)	1003 (335)	b.d.l.	b.d.l.	720 (264)	b.d.l.	5.5 (2.3)
	Augelite	Type 1	Nr	1	1	1	0	1	0	0	1	0	1	1	0	1	1	1
			Median (σ)	396 (0)	3132 (0)	31200 (0)	b.d.l.	37352 (0)	b.d.l.	b.d.l.	308 (0)	b.d.l.	1961 (0)	58 (0)	b.d.l.	426 (0)	104 (0)	7.13 (0)
		Type 2A	Nr	4	3	9	2	9	0	1	7	3	9	1	2	7	1	9
			Median (σ)	483 (38)	1154 (390)	43388 (4787)	1521 (195)	24814 (8250)	b.d.l.	39912 (0)	966 (3525)	5705 (7930)	669 (663)	6853 (0)	1921 (2616)	263 (143)	23761 (0)	6.8 (0.44)
		Type 2B	Nr	0	0	1	1	1	0	0	0	1	1	0	0	1	0	1
			Median (σ)	b.d.l.	b.d.l.	39412 (0)	1601 (0)	17377 (0)	b.d.l.	b.d.l.	b.d.l.	19426 (0)	1161 (0)	b.d.l.	b.d.l.	544 (0)	b.d.l.	5.8 (0)
		Type 3	Nr	0	0	1	0	1	0	0	0	0	1	0	0	1	0	1
			Median (σ)	b.d.l.	b.d.l.	43476 (0)	b.d.l.	19703 (0)	b.d.l.	b.d.l.	b.d.l.	b.d.l.	1278 (0)	b.d.l.	b.d.l.	371 (0)	b.d.l.	6.5 (0)

	Brazilianite	Type 1	Nr	2	2	2	1	2	0	0	1	2	2	0	1	2	0	2
			Median (σ)	127 (19.0)	248 (148)	37867 (3094)	7.1 (0)	6341 (6809)	b.d.l.	b.d.l.	82 (0)	80 (66)	258 (243)	b.d.l.	6.2 (0)	50 (38)	b.d.l.	4.46 (1.0)
		Type 2A	Nr	12	12	19	7	12	7	13	11	12	12	10	8	12	10	19
			Median (σ)	755 (705)	1232 (691)	35110 (9460)	35.2 (823)	8704 (17371)	868 (3745)	99.0 (374)	110 (665)	853 (1625)	481 (868)	3.0 (5.2)	13 (41)	141 (123)	5.5 (8.3)	4.4 (0.82)
		Type 3	Nr	1	1	1	0	1	0	0	1	1	1	0	0	1	0	1
			Median (σ)	1081 (0)	483 (0)	57544 (0)	b.d.l.	11303 (0)	b.d.l.	b.d.l.	220 (0)	182 (0)	806 (0)	b.d.l.	b.d.l.	391 (0)	b.d.l.	7.11 (0)
Quartz		Type 2A	Nr	6	7	11	8	10	1	3	8	9	8	3	3	9	3	11
			Median (σ)	452 (630)	1077 (410)	29105 (19240)	194 (3092)	15551 (13462)	32206 (0)	175 (870)	475 (1416)	4202 (26046)	918 (443)	12 (21)	100 (2109)	186 (165)	1.7 (11)	5.6 (2.8)

Nr = number of fluid inclusions showing specific element
b.d.l. = below detection limit

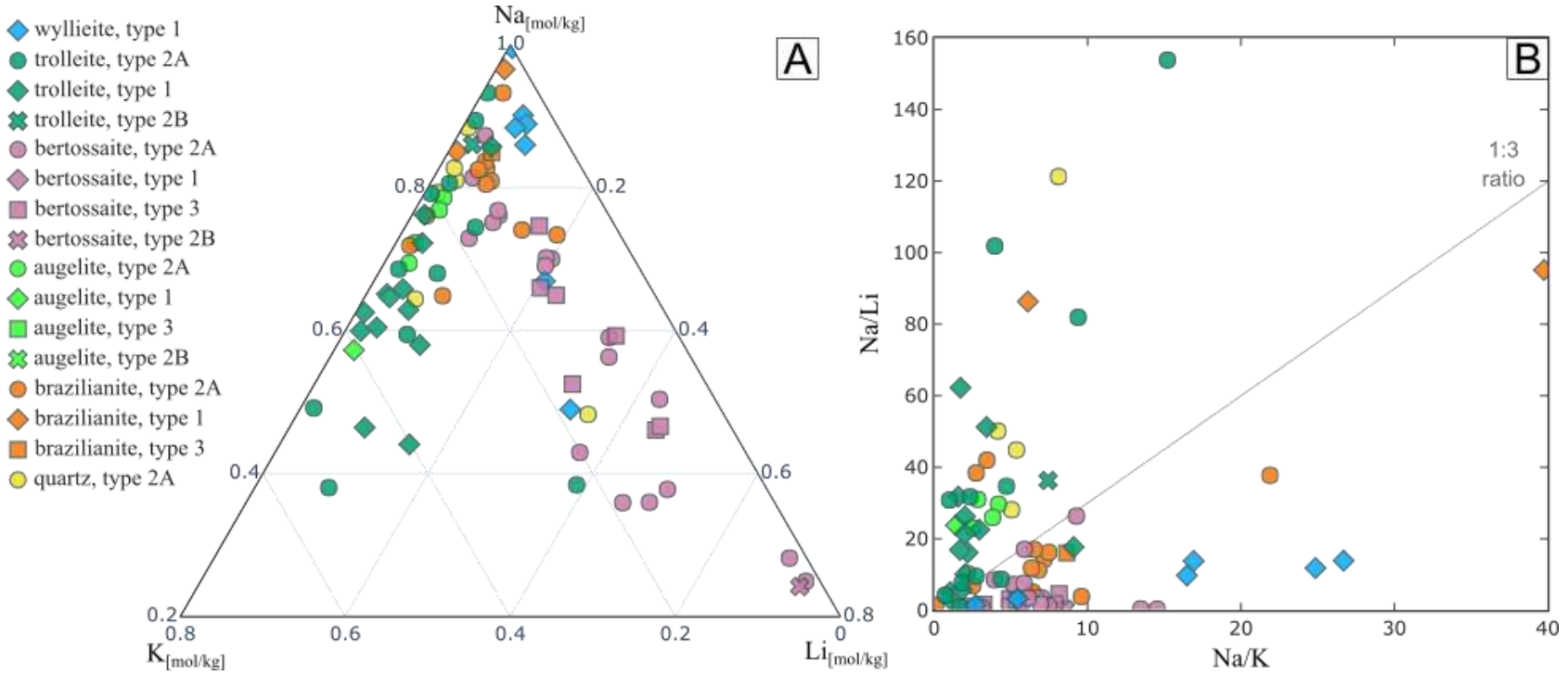


Figure 10: Relative concentrations of major alkali element solutes obtained by LA-ICPMS analyses of fluid inclusions in minerals from the Al-rich phosphatic nodules of the Buranga pegmatite. **(A)** Ternary diagram for the relative concentrations (mol/kg) of main solutes (Na, K, and Li). **(B)** Binary diagram with the ratios between the main alkali elements.

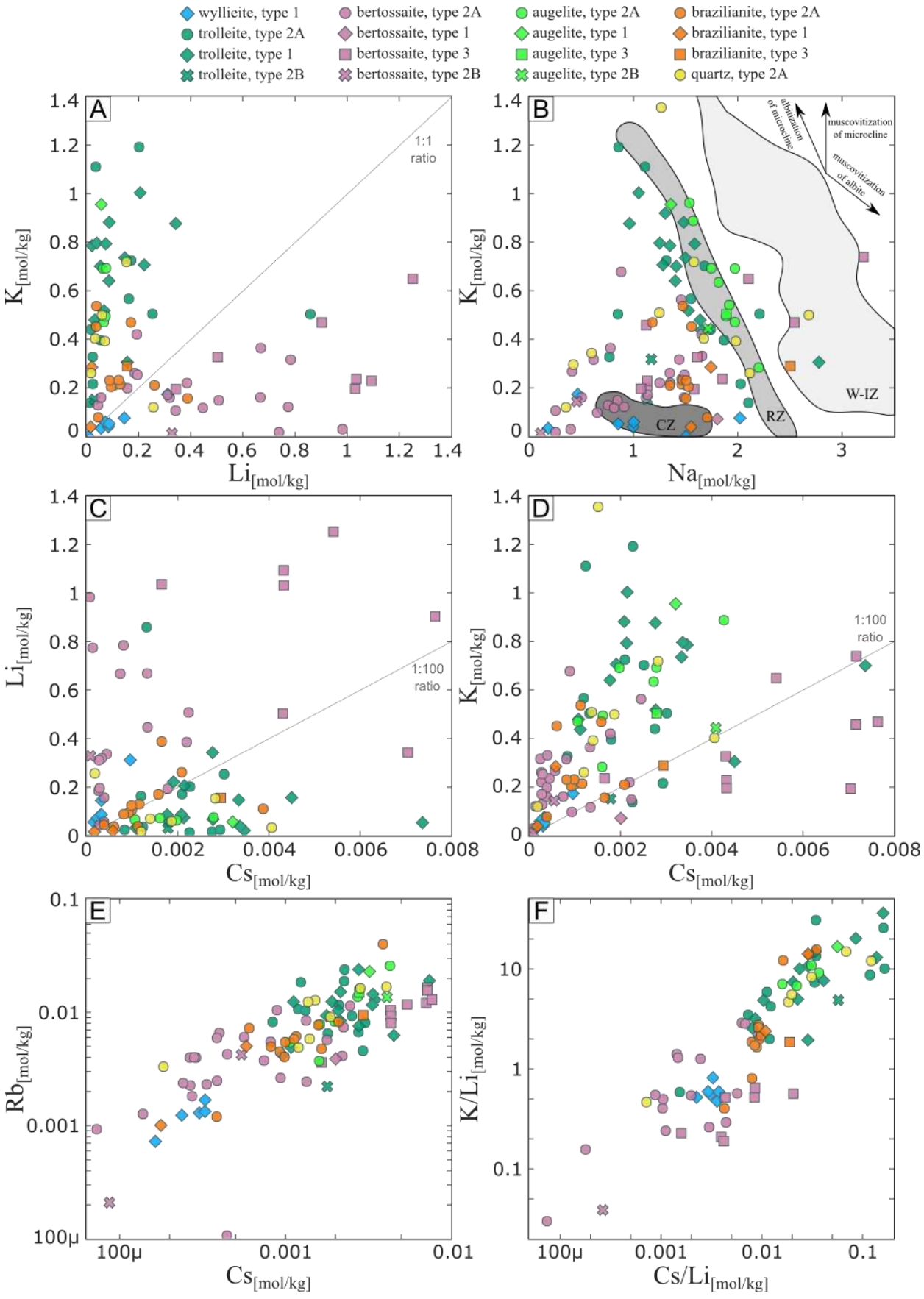


Figure 11: Binary diagrams with the correlation of the alkali elements contents (mol/kg) of fluid inclusions in minerals from the Al-rich phosphatic nodules of the Buranga pegmatite. Grey fields in B show the composition of fluid inclusions from the Gatumba dike system (Hulsbosch and Muchez, 2020); CZ = core one, RZ = replacement zone, W-IZ = wall and intermediate zones. Also shown are the vectors of typical metasomatic alterations.

5. DISCUSSION

5.1. *Pegmatitic crystallization stages*

A paragenetic sequence based on mineral replacement textures can be useful to separate subsolidus from suprasolidus replacements in pegmatitic dikes. Subsolidus replacement (i.e., hydrothermal) is pseudomorphic in nature (London and Burt, 1982), with fine-grained aggregates of one or more secondary phases crystallizing at the expense of the primary mineral (Galliski et al., 2012). This process probably occurs through interface-coupled dissolution-precipitation reactions (Ruiz-Agudo et al., 2014). Contrarily, suprasolidus replacements (magmatic/metasomatic?) occur by resorption of the primary mineral followed by precipitation of one or few large crystals of the secondary phase around it and in open spaces (Figure 2C to F). These coarse secondary phases most likely also depend on elements from the residual melt to grow, i.e., crystallizing in a three-phase system (melt-crystal-fluid).

In the Buranga pegmatite, the following crystallization stages are defined from the textural relations of phosphate minerals in previous studies (Prado Araujo et al., 2021; Prado Araujo et al., 2023): 1) magmatic stage, where wyllieite, F-rich montebrasite, rosemaryite, and trolleite precipitate from the melt due to oversaturation of their components; 2) magmatic-hydrothermal stage, where bertossaite, F-poor montebrasite, scorzalite, augelite, and brazilianite crystallize due to interactions between melt-crystal-fluid in a ternary system; 3) hydrothermal stage, where burangaite, eosphorite, samuelsonite, variscite, wardite, and other late secondary minerals crystallize by the interaction of all preceding phases with the aqueous-carbonic fluid under subsolidus conditions.

5.2. *Fluid evolution in relation to the crystallization stages*

The crystallization stages presented above serve as a foundation for the interpretation of the fluid evolution. The phosphatic sequence suggests that mineral replacements started relatively late in the timeline of dike crystallization, i.e., during formation of the Al-rich phosphatic nodules, but still at suprasolidus conditions. Furthermore, the distribution of fluid inclusions in the phosphate minerals, commonly present from the late primary minerals onwards, indicates that a magmatic fluid was widely available at least from the late magmatic stage, about at the same time as the strong

591 replacement of the primary minerals occurs. Nevertheless, the fluid phase is interpreted to be present
592 throughout the crystallization of the phosphatic nodules (fluid inclusions observed as early as
593 wyllieite).

594 The fluid trapped inside phosphate minerals in the Al-rich phosphatic nodules from the Buranga
595 dike shares many characteristics with general magmatic fluids (Audétat, 2019; Audétat and Edmonds,
596 2020). The analyzed fluid inclusions are aqueous-carbonic with a medium salinity (Figure 9), and are
597 enriched in alkali elements (Figure 10). All fluid inclusions fit into the NaCl-KCl-LiCl-H_2O-CO_2-N_2
598 system, in agreement with data from other pegmatites in the Gitarama-Gatumba field (Hulsbosch and
599 Muchez, 2020).

600 *5.2.1. Magmatic stage*

601 For the magmatic stage, the main difference is the relative increase in the contents of K, Rb, and
602 Cs, when compared to the other alkalis, in fluid inclusions from wylleite to trolleite (Figure 11). One
603 hypothesis for this behavior is that Na is an essential structural constituent of wyllieite and
604 rosemaryite, both crystallizing before trolleite. Therefore, Na is effectively a compatible element at
605 the magmatic stage. Similarly, Li behaves as a compatible element in the internal evolution of the
606 Buranga pegmatite due to F-rich montebrasite crystallization.

607 Alternatively, K, Rb, and Cs might come from exchanges between fluid and crystals
608 (metasomatism). The breakdown of K-feldspar and micas from the wall and intermediate zones
609 during albitization, i.e., a widespread process in the whole mineralized pegmatite field, could explain
610 the relative increase of K, Rb, and Cs (Hulsbosch and Muchez, 2020), since they are important
611 reservoirs for these elements (Hulsbosch et al., 2014).

612 *5.2.2. Magmatic-hydrothermal stage*

613 For the magmatic-hydrothermal stage, there is not much variation in the composition of the fluid
614 inclusions, except for the high Li content in inclusions hosted by bertossaite (Figure 10). Augelite has
615 a fluid composition somewhat similar to fluid inclusions in trolleite, whereas brazilianite records fluid
616 compositions intermediate between trolleite and bertossaite (Figure 11). These observations could
617 point to a cyclical fluid evolution at the magmatic-hydrothermal stage.

618 *5.2.3. Internal fluid evolution during crystallization*

619 In the scenario of an equilibrium crystallization, a progressive increase in the content of
620 incompatible elements is expected in the fluid composition. Specifically, there is a preferential uptake
621 of soluble elements from the melt to the fluid phase ($D_{fluid/melt} > 1$), such as B, Li, Na, Cs, Mn, Fe, W,
622 and Sn (Zajacz et al., 2008) as long as the saturation of specific minerals is not reached (e.g., pollucite
623 for Cs, cassiterite for Sn, etc.). Furthermore, when magmatic fluids are in equilibrium with crustal
624 melts (and their crystal cargo), changes in the fluid salinity are expected during crystallization
625 (Beurlen et al., 2001; Sirbescu and Nabelek, 2003b; Audétat and Edmonds, 2020). However, as
626 discussed above, these patterns are not observed in the fluid inclusions preserved in the phosphate
627 minerals. The fluid inclusion data are mostly scattered in compositional plots, without a continuous
628 trend (Figure 11), and the somewhat constant salinity (Figure 9A) indicates a fixed chlorine
629 concentration. These points suggest that an alternative process to equilibrium crystallization is in
630 action in the Buranga pegmatite. The interpretation is that the fluid composition is controlled by
631 interactions with the previous crystalline phases.

632 Changes in salinity are also expected in the case of mixing with external fluids (Mulja and
633 Williams-Jones, 2018) since both metamorphic and meteoric fluids commonly show variable salinity
634 and lower alkali content than the values obtained in this study (Whitworth and Rankin, 1989; Van
635 Daele et al., 2018; Esteves and Faleiros, 2021). The lack of CH_4 in the gaseous phase of fluid
636 inclusions (Figure 9B) suggests that the observed fluid did not re-equilibrate with the metapelitic
637 country rocks nor with fluids coming from them (Dewaele et al., 2016; Van Daele et al., 2018).

638 Combining all points, we suggest that in the case of the Al-rich phosphatic nodules from the
639 Buranga pegmatite, the aqueous-carbonic fluid phase is magmatic in origin, without clear
640 contribution from external fluids. This fluid exsolved late in the dike crystallization history, between
641 the formation of intermediate and core zones when the phosphatic nodules are formed. This late fluid
642 reacted with the primary magmatic minerals before the complete crystallization, that is, in the
643 presence of a residual melt. These melt-crystal-fluid interactions remobilized elements in the three-
644 phase system and the salinity of the fluid remained relatively constant during the magmatic-

hydrothermal stage. Fluid remobilization between different pegmatite zones is also possible (Hulsbosch and Muchez, 2020), but still limited within the dike borders. These interpretations point to a highly dynamic dike-scale system.

5.3. *Crystal-rich fluid inclusions as products of melt-crystal-fluid interactions*

The textural analysis of phosphate minerals suggests that early secondary phases precipitate after reactions between the primary minerals and the fluid, likely before the complete crystallization of the melt (Prado Araujo et al., 2023). The fluid compositional evolution along the mineral sequence supports the hypothesis that the magmatic fluid exsolved from the residual melt is in disequilibrium with the primary crystals during cooling. However, no direct evidence of this disequilibrium in the three-phase system (melt-crystal-fluid) has been discussed so far, and the nature of the residual medium is not yet clear. We suggest that crystal-rich fluid inclusions in trolleite are direct evidence of the melt-crystal-fluid interactions and provide a way to assess the residual medium during the crystallization of P-rich pegmatites.

Crystal-rich inclusions in pegmatites can represent a continuum between silicate melt inclusions, and solute-rich fluid inclusions. Commonly, these crystal-rich inclusions show a highly variable number of phases present and respective volume occupancy. These variations have been interpreted as indications of local entrapment of melt boundary layers (Bacon, 1989; Lu et al., 1995; Baker, 2008; London, 2008), immiscible melts of contrasting compositions (Frezzotti, 1992; Thomas et al., 2000; Vasyukova and Williams-Jones, 2014), heterogeneous trapping of a melt and an exsolved fluid phase (Lowenstern, 1995; Sirbescu and Nabelek, 2003b; Hulsbosch et al., 2019), or as extensive necking of inclusions after precipitation of solids due to reactions between the residual medium and host (Anderson et al., 2001; Liu et al., 2022).

Crystal-rich inclusions in trolleite from the Al-rich phosphatic nodules of Buranga show an uneven distribution of diverse phases inside the inclusions with variable occupancy proportions (Figure 6). This prevents the interpretation of solid phases as daughter minerals. Another important point to note is that some of these inclusions have rutile as a solid phase. Rutile is both present as a free phase in the groundmass and as solid inclusions in trolleite (Figure 5). Consequently, rutile is

likely an accidental solid, trapped along with the fluid when the host trolleite was crystallizing, which points to these fluid inclusions as being primary.

Those crystal-rich fluid inclusions also show a somewhat similar assemblage to the secondary phosphates replacing trolleite in the phosphatic nodules (Prado Araujo et al., 2023). Likewise, spodumene-hosted crystal-rich inclusions from other rare-element pegmatites have solid phases that are also observed in secondary mineral replacement zones (Černý, 1972; Anderson et al., 2001; Anderson, 2013; Ding et al., 2020; Liu et al., 2022). These crystal-rich inclusions have been interpreted as reaction products between the CO_2-bearing fluid and host spodumene (Anderson et al., 2001; Anderson, 2013). Moreover, crystal-rich inclusions in garnet from high-metamorphic grade rocks have been demonstrated to represent reactions between the fluid and host after entrapment, with further re-equilibration of metastable early products during cooling (Carvalho et al., 2020).

The occurrence of crystal-rich (S-L-V), crystal-poor (L-V-S), and crystal-free (L-V) primary fluid inclusions in the same inclusion field (Figure 5) indicates that the solid phases did not form in all fluid inclusions. Therefore, crystals did not precipitate from a homogeneous supersaturated fluid after entrapment (daughter crystals) nor from simple fluid - host reactions (stepdaughter crystals). Interestingly, crystal-rich inclusions in quartz (Figure 7) show different assemblages than the crystal-rich fluid inclusions in trolleite. The former contains primary phosphates, whereas trolleite contains only secondary phosphates. The fact that both minerals precipitate at similar stages, prevents the interpretation of inclusions in trolleite as pure melt inclusions. It seems that the fluid phase is trapped along with one or more phases to promote the formation of secondary phosphates within only some inclusions in the assemblage.

We suggest that crystal-rich inclusions in trolleite are products of the heterogeneous trapping of the fluid phase and the residual melt. The trapped fluid and melt subsequently react with the host mineral during cooling. This reaction caused the formation of secondary phases in the inclusions (Figure 12). The accidental trapping of primary minerals in these inclusions (along with or in place of the melt), followed by reaction with the fluid during cooling, is also a possible explanation.

Crystal-rich fluid inclusions in trolleite are the earliest robust evidence of melt-crystal-fluid interactions and confirm the existence of a three-phase system at the late crystallization stage. Therefore, these interactions mark the start of the magmatic-hydrothermal transition in the Al-rich phosphatic nodules from the Buranga pegmatite.

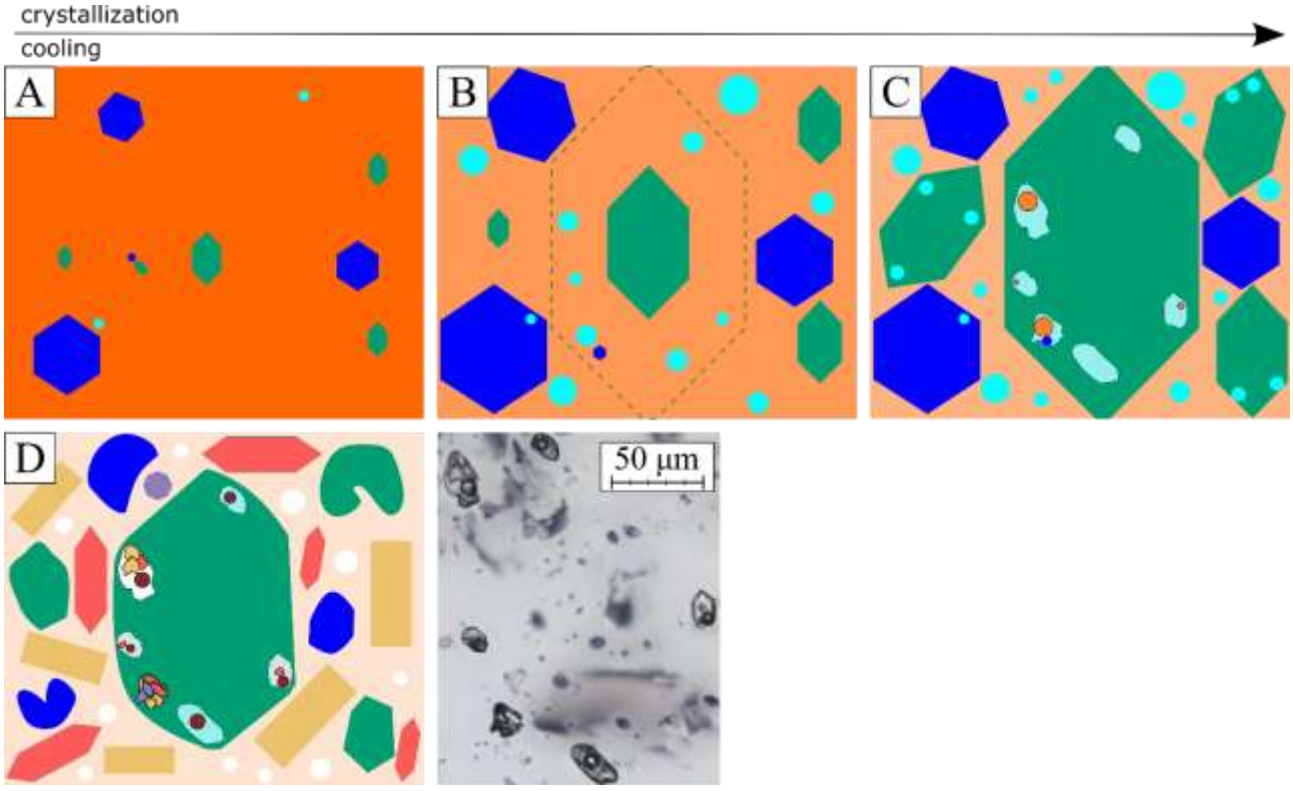


Figure 12: Schematic formation of crystal-rich inclusions. Sequence represents the heterogeneous trapping of fluid + melt (± accidental solids) in inclusions. From left to right, temperature decreases and crystallization takes place. **(A)** Primary phases (blue and green crystals) precipitate from the melt (orange background). **(B)** Widespread fluid (light blue circles) presence along with crystallization of magmatic phases. **(C)** Some fluid bubbles get trapped along with melt and accidental solids. **(D)** With further cooling, all the phases in these mixed inclusions react to generate secondary phases (yellow, pink and purple crystals), similarly to what is observed outside the inclusions and in natural fluid inclusions (image to the right).

5.4. *P-rich Rare-Element Pegmatite Petrogenesis*

The preceding discussion indicates that the fluid phase is mostly influential during the late stages of pegmatite crystallization. That is, between the consolidation of the intermediate zone and the core zone, when phosphate nodules are formed. Therefore, the model of Jahns and Burnham (1969) is not entirely applicable. The early pegmatitic melt seems to be indeed fluid-undersaturated during most of its crystallization, as shown by experimental studies (London et al., 1989; London and Morgan, 2017; Sirbescu et al., 2017). Yet, the residual melt, which is the best candidate to form the phosphatic nodules in the internal zones of the dike, is most certainly water and flux-bearing (Nabelek et al., 2010; Maneta and Baker, 2014). Fluid exsolution eventually occurs during crystallization of the

719 phosphatic nodules in the late stages of dike consolidation and directly affects the mineralogy of P-
720 rich pegmatites and rare metal mineralization (Prado Araujo et al., 2023).

721 Two models are available to explain the generation of phosphatic nodules from the water and
722 flux-bearing residual pegmatitic melt. In the first model, the fast crystallization of large crystals of
723 mostly anhydrous quartzo-feldspatic phases in the wall and intermediate zones pile up incompatible
724 and slow-diffusing elements, such as phosphorus (Baker, 2008), in the interface between the
725 crystallization front and the high viscosity haplogranitic bulk melt. This accumulation of incompatible
726 elements facilitates the development of a P-rich melt boundary layer (MBL) in the crystal-melt
727 interface by constitutional zone refining (London, 2009). When phosphate saturation is reached,
728 phosphate minerals precipitate from the MBL, and possibly remove other fluxing components (Li,
729 F), decreasing the water solubility and driving the exsolution of an aqueous phase (London, 1986;
730 London, 2014). In this case, minerals precipitating from the MBL can be in disequilibrium with both
731 the bulk melt and the fluid during cooling, which might trigger the melt-crystal-fluid interactions.

732 The second model proposes that the pegmatitic melt dissociates into two or more immiscible
733 liquids (Veksler, 2004; Thomas and Davidson, 2016). Phosphatic nodules could represent a P-rich
734 melt immiscible from the bulk silicate melt. This has been suggested due to their round to ellipsoid
735 shape, almost purely phosphatic composition, and occurrence in the pegmatite dike's core margin
736 (Roda-Robles et al., 2012a). However, experimental studies on Li-phosphate crystallization dismiss
737 the occurrence of an immiscible P-rich melt and only support the saturation of a magmatic fluid phase
738 from the residual melt (Shigley and Brown, 1986).

739 Moreover, berlinite ($AlPO_4$) is observed as a daughter mineral in melt inclusions trapped in
740 quartz precipitated from the residual peraluminous melt (Webster, 1997; Thomas and Webster, 1999),
741 sometimes without any signs of immiscibility (Veksler et al., 2003). This indicates that phosphorus
742 mostly partitions to the peraluminous silicate melt (Thomas et al., 2000; Veksler and Thomas, 2002).
743 Likewise, the Al-rich character of the studied phosphatic nodules and the observation that phosphorus
744 bonds with excess aluminum over alkalis to form $AlPO_4$ complexes in the melt (Mysen et al., 1981;

745 Mysen et al., 1997; Mysen et al., 1999) do not support the idea of a P-rich immiscible melt (from an
746 aluminosilicate bulk melt).

747 Melt-melt immiscibility is normally observed in experiments with peralkaline melts (Veksler et
748 al., 2012), whereas the two-melt immiscibility field is not commonly reached by experimental
749 peraluminous melts (Veksler, 2004; Dolejš and Baker, 2007; Van Lichtervelde et al., 2021). P-rich
750 melt immiscibility might be triggered by processes that destabilize the strong Al-P complexes in the
751 melt, such as high Ca content (Van Lichtervelde et al., 2021) or high concentrations of F and B
752 (London et al., 1999). However, all of these elements are present in low quantities in the Buranga
753 pegmatite. Similarly, considering that two types of phosphatic nodules (Al-rich and Fe-Mn-rich)
754 occur separately but in near proximity in the Buranga dike, more than one P-rich immiscible melt
755 would be required. Multiple P-rich immiscible melts are not expected to form from a single
756 peraluminous bulk melt.

757 We propose that the Al-rich phosphatic nodules from the inner zones of the Buranga pegmatite
758 crystallized from a residual P-rich melt after extensive crystallization, both regionally, from source
759 to emplacement, and locally, from margins to the center of the dike. The pegmatitic melt was
760 progressively enriched in water and other fluxing components (Li, P, B, F, etc.). The fluid phase
761 exsolves from the residual melt due to extended crystallization of anhydrous and flux-bearing
762 minerals, possibly kinetically aided by their fast growth (Sirbescu et al., 2017; Hulsbosch and
763 Muchez, 2020). The formation of the P-rich melt from a concentrated melt boundary layer seems to
764 be the more straightforward process, whereas its origin by immiscibility from the bulk silicate melt
765 seems unlikely. Nevertheless, the precise mechanism generating the phosphatic nodules is not yet
766 clear and more studies are required for a definite answer.

767 ### 5.5. *Nb-Ta Ore Metallogenesis*

768 Rare metal deposits (Nb, Ta, Li, Be, Sn, W) are commonly present in highly evolved lithophile-
769 enriched granites and pegmatites, also known as rare metal granitoids (Pollard, 1995 and references
770 therein). The concentration of such elements in the melt is explained by protracted fractional
771 crystallization, both regionally from source to emplacement and internally during solidification

(Černý et al., 1985; Raimbault et al., 1995; Prado Araujo et al., 2020). However, the concentration of rare metals in pegmatitic melts (Webster et al., 1997; Borisova et al., 2012), certainly the most differentiated in the magmatic series, is commonly below the saturation point for most ore minerals (Linnen and Keppler, 1997; Linnen, 1998; Van Lichtervelde et al., 2018; London, 2018; McNeil et al., 2020).

Some studies propose that the mineralization is still magmatic, and that ore precipitation occurs due to extreme undercooling and disequilibrium crystallization (Van Lichtervelde et al., 2018; London, 2018) or chemical quenching (Linnen et al., 2012). Contrarily, others suggest that the metal content is concentrated in the residual melt, but precipitation occurs after remobilization by a fluid phase (Michaud et al., 2020; Ballouard et al., 2020; Kaeter et al., 2021) .

In the Al-rich phosphatic nodules from the Buranga pegmatite, the precipitation of columbite-group minerals (CGM) is associated with the fluid-mediated alteration of primary minerals and the precipitation of secondary phosphates (Prado Araujo et al., 2023). This agrees with the propositions that the mineralization follows the remobilization by a fluid phase.

Overall, a high salinity fluid, more saline than most of the inclusions observed in this study, is needed to mobilize the metals (Yardley, 2005; Audétat et al., 2008). The measured concentrations of Nb and Ta in the fluid inclusions is indeed low (below 100 ppm - Table 4), indicating that these are not mobilized by the fluid phase. However, the observed fluid inclusions contain considerable amounts of Fe and Mn (a few thousand ppm - Table 4), which are also essential structural constituents of CGM.

These results suggest that the fluid is mostly responsible for mobilizing the soluble Fe and Mn, whereas the residual melt provides Nb and Ta for mineralization. The fluid phase, being less viscous and more mobile than the silicate melt, is more effective in migrating between different assemblages, altering crystalline phases, and remobilizing the required elements. Likewise, mineral textures are more indicative of the reaction with a fluid phase (Prado Araujo et al., 2023), and this corroborates experimental observations that melt-fluid interactions are responsible for CGM mineralization

(McNeil et al., 2020). Consequently, a back-reaction of the primary phases with the residual melt to liberate the Fe and Mn content at the magmatic-hydrothermal stage is not supported.

Combining all observations, a mineralization model is proposed for the Buranga pegmatite and similar P-rich rare-element LCT pegmatites. At the magmatic stage, the melt becomes progressively enriched in incompatible elements, including Nb and Ta, but the low availability of Fe-Mn in the melt due to their uptake by primary phosphates inhibits the saturation of CGM. At the late magmatic stage, the melt becomes saturated in an aqueous-carbonic fluid (magmatic-hydrothermal stage). This fluid reacts with the earlier magmatic phases and internally remobilizes fluid-soluble elements (e.g., Fe and Mn). These elements are again available to combine with the residual melt and locally precipitate CGM and secondary phosphates around the consumed magmatic phases.

6. CONCLUSIONS

This study shows that the investigation of complex phosphatic mineral assemblages and their fluid inclusion record can provide meaningful information about the internal processes of pegmatitic dikes. The analyzed fluids belong to a single compositional system, NaCl-KCl-LiCl-H_2O-CO_2-N_2, and generally show a high content of alkali elements. Additionally, the salinity of analyzed inclusions is somewhat constant in all studied minerals (10-20 $NaCl_{eq.}$ mass%, median at 13.8 ± 3.1 $NaCl_{eq.}$ mass%). The chemical variations during the magmatic and magmatic-hydrothermal stages do not fit an equilibrium crystallization model, but rather show a cyclical behavior of increasing and decreasing alkali element ratios (e.g., K/Li, Rb/Li, Cs/Li, K/Rb, K/Cs, etc.) during the paragenetic sequence. This hints at a fluid evolution constrained by interactions with the magmatic phases, e.g., wyllieite, F-rich montebrasite, rosemaryite, trolleite, and silicates at suprasolidus conditions.

Crystal-rich fluid inclusions in trolleite are the best examples of such interactions. These inclusions are interpreted as the heterogeneous trapping of the aqueous-carbonic fluid, the residual melt (with its crystal cargo as accidentally trapped solids) and primary solids. The occurrence of late secondary phases inside these inclusions suggests that the fluid continues to react with the magmatic phases as the temperature decreases. Consequently, a single aqueous-carbonic fluid exsolved from

the melt likely generates all the secondary phases observed in the phosphatic nodules by reacting with earlier minerals. No evidence of the influx of external fluids or fluid mixing is observed in the magmatic-hydrothermal transition stage. Nevertheless, this magmatic fluid could have interacted with surrounding pegmatitic mineral assemblages (silicates and Fe-Mn phosphates) and remobilized alkalis and other fluid-mobile elements (Fe,Mn) between the dike zones.

The combined results and interpretations of this study suggest that fluids hold an important role in the late magmatic crystallization of pegmatitic melts and associated Nb-Ta mineralization. An aqueous-carbonic fluid exsolves from the residual melt before complete crystallization. The remobilization of elements due to melt-crystal-fluid interactions during the magmatic-hydrothermal transition enables the mineralization of Nb-Ta-oxide minerals and secondary phosphate minerals, some of which are Li-bearing minerals (montebrasite and bertossaite) or uncommon gemstones (brazilianite).

ACKNOWLEDGMENTS

This research was financially supported by the KU Leuven Research Fund (Grant C14/17/056). FPA was funded by a PhD scholarship from KU Leuven. Research of NH was supported by a Junior Postdoctoral Fellowship of the FWO. The Raman equipment of KU Leuven was acquired via the medium-scale research infrastructure grant Raman-SIM2 (grant no I000718N). This manuscript was improved by the constructive comments from two anonymous reviewers and the associate editor, Zoltan Zajacz. The authors are grateful to Stijn Dewaele (UGent), Florias Mees (Royal Museum for Central Africa), and Frédéric Hatert (ULiège) for providing the Buranga samples and fruitful discussions. Herman Nijs (KU Leuven) is thanked for preparing the wafers. The support of Marie-Christine Boiron and Chantal Peiffert (Université de Lorraine, CNRS, CREGU) in the LA-ICPMS analyses and related discussions is highly appreciated. An earlier version of this manuscript, in the form of a chapter in the PhD thesis of FPA, benefited from discussions and comments from Olivier Namur, Jan Elsen, Marieke Van Lichtervelde and Frédéric Hatert. Philippe Muchez, Niels Hulsbosch,

and Fernando Prado Araujo are members of the KU Leuven Institute for Sustainable Metals and Minerals.

RESEARCH DATA

Research Data associated with this article are deposited in the KU Leuven Research Data Repository (RDR) and can be accessed at https://doi.org/10.48804/QEBXIC.

REFERENCES

Alfonso P. and Melgarejo J.-C. (2008) Fluid evolution in the zoned rare-element pegmatite field at Cap de Creus, Catalonia, Spain. *Can. Mineral.* **46**, 597–617.

Allan M. M., Yardley B. W. D., Forbes L. J., Shmulovich K. I., Banks D. A. and Shepherd T. J. (2005) Validation of LA-ICP-MS fluid inclusion analysis with synthetic fluid inclusions. *Am. Mineral.* **90**, 1767–1775.

Anderson A. J. (2013) Are silicate-rich inclusions in spodumene crystallized aliquots of boundary layer melt? *Geofluids* **13**, 460–466.

Anderson A. J., Clark A. H. and Gray S. (2001) The occurrence and origin of zabuyelite (Li_2CO_3) in spodumene-hosted fluid inclusions: Implications for the internal evolution of rare-element granitic pegmatites. *Can. Mineral.* **39**, 1513–1527.

Ashworth L., Kinnaird J. A., Andrew P., Nex M., Erasmus R. M. and Józef W. (2018) Characterization of fluid inclusions from mineralized pegmatites of the Damara Belt , Namibia : insight into late-stage fluid evolution and implications for mineralization. *Mineral. Petrol.* **112**, 753–765.

Audétat A. (2019) The Metal Content of Magmatic-Hydrothermal Fluids and Its Relationship to Mineralization Potential. *Econ. Geol.* **114**, 1033–1056.

Audétat A. and Edmonds M. (2020) Magmatic-Hydrothermal Fluids. *Elements* **16**, 401–406.

Audétat A., Pettke T., Heinrich C. A. and Bodnar R. J. (2008) Special paper: The composition of magmatic-hydrothermal fluids in barren and mineralized intrusions. *Econ. Geol.* **103**, 877–908.

878 Bacon C. R. (1989) Crystallization of accessory phases in magmas by local saturation adjacent to
879 phenocrysts. *Geochim. Cosmochim. Acta* **53**, 1055–1066.
880 Baijot M., Hatert F., Dal Bo F. and Philippo S. (2014) Mineralogy and petrography of phosphate
881 mineral associations from the Jocão pegmatite, Minas Gerais, Brazil. *Can. Mineral.* **52**, 373–
882 397.
883 Baker D. R. (2008) The fidelity of melt inclusions as records of melt composition. *Contrib. Mineral.*
884 *Petrol.* **156**, 377–395.
885 Ballouard C., Massuyeau M., Elburg M. A., Tappe S., Viljoen F. and Brandenburg J.-T. (2020) The
886 magmatic and magmatic-hydrothermal evolution of felsic igneous rocks as seen through Nb-Ta
887 geochemical fractionation, with implications for the origins of rare-metal mineralizations. *Earth-*
888 *Science Reviews* **203**, 103115.
889 Barros R. and Menuge J. F. (2016) The origin of spodumene pegmatites associated with the leinster
890 granite in southeast Ireland. *Can. Mineral.* **54**, 847–862.
891 Bartels A., Vetere F., Holtz F., Behrens H. and Linnen R. L. (2011) Viscosity of flux-rich pegmatitic
892 melts. *Contrib. Mineral. Petrol.* **162**, 51–60.
893 Behrens H., Meyer M., Holtz F., Benne D. and Nowak M. (2001) The effect of alkali ionic radius,
894 temperature, and pressure on the solubility of water in $MAlSi_3O_8$ melts (M=Li, Na, K, Rb).
895 *Chem. Geol.* **174**, 275–289.
896 Bettencourt J. S., Leite W. B., Goraieb C. L., Sparrenberger I., Bello R. M. da S. and Payolla B. L.
897 (2005) Sn-polymetallic greisen-type deposits associated with late-stage rapakivi granites, Brazil:
898 Fluid inclusion and stable isotope characteristics. *Lithos* **80**, 363–386.
899 Beurlen H., Silva M. R. R. D. A. and Castro C. De (2001) Fluid inclusion microthermometry in Be-
900 Ta-(Li-S) -bearing pegmatites from the Borborema Province, Northeast Brazil. *Chem. Geol.* **173**,
901 107–123.
902 Borisova A. Y., Thomas R., Salvi S., Candaudap F., Lanzanova A. and Chmeleff J. (2012) Tin and
903 associated metal and metalloid geochemistry by femtosecond LA-ICP-QMS microanalysis of
904 pegmatite–leucogranite melt and fluid inclusions: new evidence for melt–melt–fluid

immiscibility. *Mineral. Mag.* **76**, 91–113.

Burke E. A. J. (2001) Raman microspectrometry of fluid inclusions. *Lithos* **55**, 139–158.

Cameron E. ., Jahns R. H., McNair A. H. and Page L. R. (1949) *Internal structure of granitic pegmatites*., Economic Geology Publishing Co, Urbana.

Carvalho B. B., Bartoli O., Cesare B., Tacchetto T., Gianola O., Ferri F., Aradi L. E. and Szabó C. (2020) Primary CO_2-bearing fluid inclusions in granulitic garnet usually do not survive. *Earth and Planetary Science Letters* **536**, 116170.

Černý P. (1972) The Tanco Pegmatite at Bernic Lake, Manitoba. VIII. Secondary minerals from the spodumene-rich zones. *Can. Mineral.* **11**, 714–726.

Černý P., Meintzer R. E. and Anderson A. J. (1985) Extreme fractionation in rare-element granitic pegmatites: selected examples of data and mechanisms. *Can. Mineral.* **23**, 381–421.

Van Daele J., Hulsbosch N., Dewaele S., Boiron M.-C., Piessens K., Boyce A. and Muchez P. (2018) Mixing of magmatic-hydrothermal and metamorphic fluids and the origin of peribatholitic Sn vein-type deposits in Rwanda. *Ore Geol. Rev.* **101**, 481–501.

Van Daele J., Hulsbosch N., Dewaele S. and Muchez P. (2020) Metamorphic and metasomatic evolution of the Western Domain of the Karagwe-Ankole Belt (Central Africa). *J. Afr. Earth Sci.* **165**, 103783.

Daltry V. D. C. and von Knorring O. (1998) Type-mineralogy of Rwanda with particular reference to the Buranga pegmatite. *Geol. Belg.* **1**, 9–15.

Darling R. S. (1991) An extended equation to calculate NaCl contents from final clathrate melting temperatures in H_2O-CO_2-NaCl fluid inclusions: Implications for P-T isochore location. *Geochim. Cosmochim. Acta* **55**, 3869–3871.

Dewaele S., De Clercq F., Hulsbosch N., Piessens K., Boyce A., Burgess R. and Muchez P. (2016) Genesis of the vein-type tungsten mineralization at Nyakabingo (Rwanda) in the Karagwe–Ankole belt, Central Africa. *Mineralium Deposita* **51**, 283–307.

Dewaele S., Henjes-Kunst F., Melcher F., Sitnikova M., Burgess R., Gerdes A., Fernandez-Alonso M., de Clercq F., Muchez P. and Lehmann B. (2011) Late Neoproterozoic overprinting of the

cassiterite and columbite-tantalite bearing pegmatites of the Gatumba area, Rwanda (Central Africa). *J. Afr. Earth Sci.* **61**, 10–26.

Diamond L. W. (2001) Review of the systematics of CO_2 – H_2O fluid inclusions. *Lithos* **55**, 69–99.

Ding X., Li J., Chou I. M., Chen Z. and Li S. (2020) Raman spectroscopic identification of cookeite in the crystal-rich inclusions in spodumene from the Jiajika lithium pegmatite deposit, China, and its geological implications. *Eur. J. Mineral.* **32**, 67–75.

Dingwell D. B., Holtz F. and Behrens H. (1997) The solubility of H_2O in peralkaline and peraluminous granitic melts. *Am. Mineral.* **82**, 434–437.

Dingwell D. B., Knoche R. and Webb S. L. (1993) The effect of P_2O_5 on the viscosity of haplogranitic liquid. *Eur. J. Mineral.* **5**, 133–140.

Dolejš D. and Baker D. R. (2007) Liquidus Equilibria in the System K_2O-Na_2O-Al_2O_3-SiO_2-F_2O_{-1}-H_2O to 100 MPa: I. Silicate-Fluoride Liquid Immiscibility in Anhydrous Systems. *J. Petrol.* **48**, 785–806.

Dubois M., Monnin C., Castelain T., Coquinot Y., Gouy S., Gauthier A. and Goffe B. (2010) Investigation of the H2O-NaCl-LiCl System: A Synthetic Fluid Inclusion Study and Thermodynamic Modeling from −50 ° to +100 °C and up to 12 mol/kg. *Econ. Geol.* **105**, 329–338.

Esteves M. C. B. and Faleiros F. M. (2021) Fluid flow and syntectonic veining in an Ediacaran-Cambrian foreland fold–thrust zone, western margin of the São Francisco Craton, Brazil. *Journal of the Geological Society* **178**, jgs2020-061.

Fernandez-Alonso M., Cutten H., De Waele B., Tack L., Tahon A., Baudet D. and Barritt S. D. (2012) The Mesoproterozoic Karagwe-Ankole Belt (formerly the NE Kibara Belt): The result of prolonged extensional intracratonic basin development punctuated by two short-lived far-field compressional events. *Precambrian Research* **216**–**219**, 63–86.

Fisher D. J. (1958) Pegmatite phosphates and their problems. *Am. Mineral.* **43**, 181–207.

Fransolet A.-M. (1975) Etude minéralogique et pétrologique des phosphates de pegmatites granitiques. Fascicule I: Texte. 333 p. Ph.D. thesis, University of Liège, Liège. (in French).

Fransolet A.-M., Keller P. and Fontan F. (1986) The phosphate mineral associations of the Tsaobismund pegmatite, Namibia. *Contrib. Mineral. Petrol.* **92**, 502–517.

Frezzotti M. L. (1992) Magmatic immiscibility and fluid phase evolution in the Mount Genis granite (southeastern Sardinia, Italy). *Geochim. Cosmochim. Acta* **56**, 21–33.

Fuchsloch W. C., Nex P. A. M. and Kinnaird J. A. (2018) Classification, mineralogical and geochemical variations in pegmatites of the Cape Cross-Uis pegmatite belt, Namibia. *Lithos* **296**–**299**, 79–95.

Galliski M. Á., Černý P., Márquez-Zavalía M. F. and Chapman R. (2012) An association of secondary Al-Li-Be-Ca-Sr phosphates in the San Elías pegmatite, San Luis, Argentina. *Can. Mineral.* **50**, 933–942.

Galliski M. Á., Roda-Robles E., Hatert F., Márquez-Zavalía M. F. and Martínez V. A. (2020) The Phosphate mineral assemblages from La Viquita Pegmatite, San Luis, Argentina. *Can. Mineral.* **58**, 733–746.

Gammel E. M. and Nabelek P. I. (2016) Fluid inclusion examination of the transition from magmatic to hydrothermal conditions in pegmatites from San Diego County, California. *Am. Mineral.* **101**, 1906–1915.

Guillong M., Meier D. L., Allan M. M., Heinrich C. A. and Yardley B. W. D. (2008) SILLS: A Matlab-Based Program for the Reduction of Laser Ablation ICP–MS Data of Homogeneous Materials and Inclusions. *Mineralogical Association of Canada Short Course* **40**, 328–333.

Harlov D. E. (2015) Apatite: A fingerprint for metasomatic processes. *Elements* **11**, 171–176.

Holtz F., Dingwell D. B. and Behrens H. (1993) Effects of F, B_2O_3 and P_2O_5 on the solubility of water in haplogranite melts compared to natural silicate melts. *Contrib. Mineral. Petrol.* **113**, 492–501.

Hulsbosch N. (2019) Nb-Ta-Sn-W Distribution in Granite-related Ore Systems. In *Ore Deposits: Origin, Exploration, and Exploitation* (eds. S. Decrée and L. J. Robb). pp. 75–107.

Hulsbosch N., Boiron M.-C., Dewaele S. and Muchez P. (2016) Fluid fractionation of tungsten during granite-pegmatite differentiation and the metal source of peribatholitic W quartz veins: Evidence

from the Karagwe-Ankole Belt (Rwanda). *Geochim. Cosmochim. Acta* **175**, 299–318.

Hulsbosch N., Boiron M.-C., Thomas R., Van Daele J., Dewaele S. and Muchez P. (2019) Evaluation of the petrogenetic significance of melt inclusions in pegmatitic schorl-dravite from graphic tourmaline-quartz assemblages: Application of LA-ICP-QMS analyses and volume ratio calculations. *Geochim. Cosmochim. Acta* **244**, 308–335.

Hulsbosch N., Hertogen J., Dewaele S., André L. and Muchez P. (2014) Alkali metal and rare earth element evolution of rock-forming minerals from the Gatumba area pegmatites (Rwanda): Quantitative assessment of crystal-melt fractionation in the regional zonation of pegmatite groups. *Geochim. Cosmochim. Acta* **132**, 349–374.

Hulsbosch N. and Muchez P. (2020) Tracing fluid saturation during pegmatite differentiation by studying the fluid inclusion evolution and multiphase cassiterite mineralisation of the Gatumba pegmatite dyke system (NW Rwanda). *Lithos* **354**–**355**, 105285.

Jahns R. H. and Burnham C. W. (1969) Experimental studies of pegmatite genesis. I: A model for the derivation and crystallization of granitic pegmatites. *Econ. Geol.* **64**, 843–864.

Kaeter D., Barros R. and Menuge J. F. (2021) Metasomatic high field strength element, tin, and base metal enrichment processes in lithium pegmatites from Southeast Ireland. *Econ. Geol.* **116**, 169–198.

Van Den Kerkhof A. M. and Hein U. F. (2001) Fluid inclusion petrography. *Lithos* **55**, 27–47.

Van Den Kerkhof A. M. and Thiéry R. (2001) Carbonic inclusions. *Lithos* **55**, 49–68.

Van Lichtervelde M., Goncalves P., Eglinger A., Colin A., Montel J.-M. and Dacheux N. (2021) Solubility of Monazite–Cheralite and Xenotime in Granitic Melts, and Experimental Evidence of Liquid–Liquid Immiscibility in Concentrating REE. *J. Petrol.* **62**, 1–20.

Van Lichtervelde M., Holtz F. and Melcher F. (2018) The effect of disequilibrium crystallization on Nb-Ta fractionation in pegmatites: Constraints from crystallization experiments of tantalite-tapiolite. *Am. Mineral.* **103**, 1401–1416.

Linnen R. L. (1998) The solubility of Nb-Ta-Zr-Hf-W in granitic melts with Li and Li + F: Constraints for mineralization in rare metal granites and pegmatites. *Econ. Geol.* **93**, 1013–1025.

Linnen R. L. and Keppler H. (1997) Columbite solubility in granitic melts: Consequences for the enrichment and fractionation of Nb and Ta in the Earth's crust. *Contrib. Mineral. Petrol.* **128**, 213–227.

Linnen R. L., Van Lichtervelde M. and Černý P. (2012) Granitic pegmatites as sources of strategic metals. *Elements* **8**, 275–280.

Linnen R. L., McNeil A. G. and Flemming R. (2019) Some thoughts on metasomatism in pegmatites. *Can. Mineral.* **57**, 765–766.

Liu Y., Schmidt C. and Li J. (2022) Peralkalinity in peraluminous granitic pegmatites. II. Evidence from experiments on carbonate formation in spodumene-bearing assemblages. *Am. Mineral.* **107**, 239–247.

Llorens T. and Moro M. C. (2012) Fe-Mn phosphate associations as indicators of the magmatic-hydrothermal and supergene evolution of the Jálama batholith in the Navasfrías Sn-W District, Salamanca, Spain. *Mineral. Mag.* **76**, 1–24.

London D. (2014) A petrologic assessment of internal zonation in granitic pegmatites. *Lithos* **184**–**187**, 74–104.

London D. (2022) A Rayleigh model of cesium fractionation in granite-pegmatite systems. *Am. Mineral.* **107**, 82–91.

London D. (1987) Internal differentiation of rare-element pegmatites: Effects of boron, phosphorus, and fluorine. *Geochim. Cosmochim. Acta* **51**, 403–420.

London D. (1986) Magmatic-hydrothermal transition in the Tanco rare-element pegmatite: evidence from fluid inclusions and phase-equilibrium experiments. *Am. Mineral.* **71**, 376–395.

London D. (2018) Ore-forming processes within granitic pegmatites. *Ore Geol. Rev.* **101**, 349–383.

London D. (2008) Pegmatites. *The Canadian Mineralogist. Special Publication* **10**, 347 p.

London D. (2015) Reply to Thomas and Davidson on "A petrologic assessment of internal zonation in granitic pegmatites" (London, 2014a). *Lithos* **212**–**215**, 469–484.

London D. (2009) The Origin of Primary Textures in Granitic Pegmatites. *Can. Mineral.* **47**, 697–724.

London D. and Burt D. M. (1982) Alteration of spodumene, montebrasite and lithiophilite in pegmatites of the White Picacho district, Arizona. *Am. Mineral.* **67**, 97–113.

London D. and Morgan G. B. V. (2017) Experimental crystallization of the Macusani Obsidian, with applications to lithium-rich granitic pegmatites. *J. Petrol.* **58**, 1005–1030.

London D., Morgan G. B. V., Babb H. A. and Loomis J. L. (1993) Behavior and effects of phosphorus in the system Na_2O-K_2O-Al_2O_3-SiO_2-P_2O_5-H_2O at 200 MPa(H_2O). *Contrib. Mineral. Petrol.* **113**, 450–465.

London D., Morgan G. B. V. and Hervig R. L. (1989) Vapor-undersaturated experiments with Macusani glass+H_2O at 200 MPa, and the internal differentiation of granitic pegmatites. *Contrib. Mineral. Petrol.* **102**, 1–17.

London D., Morgan G. B. V. and Wolf M. B. (2001) Amblygonite-montebrasite solid solutions as monitors of fluorine in evolved granitic and pegmatitic melts. *Am. Mineral.* **86**, 225–233.

London D., Wolf M. B., Morgan G. B. V. and Garrido M. G. (1999) Experimental silicate-phosphate equilibria in peraluminous granitic magmas, with a case study of the Alburquerque batholith at Tres Arroyos, Badajoz, Spain. *J. Petrol.* **40**, 215–240.

Lowenstern J. B. (1995) Application of Silicate-Melt Inclusions to the Study of Magmatic Volatiles. In *Magmas, fluids and ore deposits* (ed. J. F. H. Thompson). Mineralogical Association of Canada Short Course Series 23, Quebec. pp. 71–99.

Lu F., Anderson A. T. and Davis A. M. (1995) Diffusional Gradients at the Crystal/Melt Interface and Their Effect on the Compositions of Melt Inclusions. *The Journal of Geology* **103**, 591–597.

Lu J. and Lottermoser B. G. (1997) Petrogenesis of rare-element pegmatites in the Olary Block, South Australia, part 2. Fluid inclusion study. *Mineral. Petrol.* **59**, 21–41.

Maneta V. and Baker D. R. (2014) Exploring the effect of lithium on pegmatitic textures: An experimental study. *Am. Mineral.* **99**, 1383–1403.

McNeil A. G., Linnen R. L., Flemming R. L. and Fayek M. (2020) An experimental approach to examine fluid-melt interaction and mineralization in rare-metal pegmatites. *Am. Mineral.* **105**, 1078–1087.

Melcher F., Graupner T., Gäbler H.-E., Sitnikova M., Henjes-Kunst F., Oberthür T., Gerdes A. and Dewaele S. (2015) Tantalum-(niobium-tin) mineralisation in African pegmatites and rare metal granites: Constraints from Ta-Nb oxide mineralogy, geochemistry and U-Pb geochronology. *Ore Geol. Rev.* **64**, 667–719.

Michallik R. M., Wagner T. and Fusswinkel T. (2020) Late-stage fluid exsolution and fluid phase separation processes in granitic pegmatites: Insights from fluid inclusion studies of the Luumäki gem beryl pegmatite (SE Finland). *Lithos* **380**–**381**, 105852.

Michaud J. A. S., Gumiaux C., Pichavant M., Gloaguen E. and Marcoux E. (2020) From magmatic to hydrothermal Sn-Li-(Nb-Ta-W) mineralization: The Argemela area (central Portugal). *Ore Geol. Rev.* **116**, 103215.

Michaud J. A. S. and Pichavant M. (2020) Magmatic fractionation and the magmatic-hydrothermal transition in rare metal granites: Evidence from Argemela (Central Portugal). *Geochim. Cosmochim. Acta* **289**, 130–157.

Moore P. B. (1973) Pegmatite phosphates: descriptive mineralogy and crystal chemistry. *Mineral. Rec.* **4**, 103–130.

Muchez P., Hulsbosch N. and Dewaele S. (2014) Geological mapping and implications for Nb-Ta, Sn and W prospection in Rwanda. *Mededelingen Zittingen Koninklijke Academie Overzeese Wetenschappen* **60**, 515–530.

Mulja T. and Williams-Jones A. E. (2018) The physical and chemical evolution of fluids in rare-element granitic pegmatites associated with the Lacorne pluton, Québec, Canada. *Chem. Geol.* **493**, 281–297.

Müller A., Romer R. L. and Pedersen R. B. (2017) The sveconorwegian pegmatite province - thousands of pegmatites without parental granites. *Can. Mineral.* **55**, 283–315.

Mysen B. O., Holtz F., Pichavant M., Beny J.-M. and Montel J.-M. (1997) Solution mechanisms of phosphorus in quenched hydrous and anhydrous granitic glass as a function of peraluminosity. *Geochim. Cosmochim. Acta* **61**, 3913–3926.

Mysen B. O., Holtz F., Pichavant M., Beny J. M. and Montel J. M. (1999) The effect of temperature

and bulk composition on the solution mechanism of phosphorus in peraluminous haplogranitic magma. *Am. Mineral.* **84**, 1336–1345.

Mysen B. O., Ryerson F. J. and Virgo D. (1981) The structural role of phosphorus in silicate melts. *Am. Mineral.* **66**, 106–117.

Nabelek P. I., Whittington A. G. and Sirbescu M.-L. C. (2010) The role of H_2O in rapid emplacement and crystallization of granite pegmatites: Resolving the paradox of large crystals in highly undercooled melts. *Contrib. Mineral. Petrol.* **160**, 313–325.

Pettke T., Oberli F., Audétat A., Guillong M., Simon A. C., Hanley J. J. and Klemm L. M. (2012) Recent developments in element concentration and isotope ratio analysis of individual fluid inclusions by laser ablation single and multiple collector ICP-MS. *Ore Geol. Rev.* **44**, 10–38.

Pichavant M. (1983) Melt-fluid interaction deduced from studies of silicate-B_2O_3-H_2O systems at 1 kbar. *Bulletin de Minéralogie* **106**, 201–211.

Pirard C., Hatert F. and Fransolet A.-M. (2007) Alteration sequences of aluminium phosphates from Montebras Pegmatite, Massif Central, France. *Granitic Pegmatites: The State of the Art – International Symposium. 06th – 12th May 2007, Porto, Portugal.*, 1.

Pohl W. L., Biryabarema M. and Lehmann B. (2013) Early Neoproterozoic rare metal (Sn, Ta, W) and gold metallogeny of the Central Africa Region: a review. *Appl. Earth Sci.* **122**, 66–82.

Polinard E. (1950) La montebrasite de Buranga. In *Troisième Congrès National des Sciences (Bruxelles)* Brussels. pp. 18-19. (in French).

Pollard P. J. (1995) A special issue devoted to the geology of rare metal deposits: an introduction and overview. *Econ. Geol.* **90**, 489–494.

Pollard P. J., Andrew A. S. and Taylor R. G. (1991) Fluid inclusion and stable isotope evidence for interaction between granites and magmatic hydrothermal fluids during formation of disseminated and pipe-style mineralization at the Zaaiplaats tin mine. *Econ. Geol.* **86**, 121–141.

Prado Araujo F., Hulsbosch N. and Muchez P. (2021) High spatial resolution Raman mapping of complex mineral assemblages: Application on phosphate mineral sequences in pegmatites. *J. Raman Spectrosc.* **52**, 690–708.

Prado Araujo F., Hulsbosch N. and Muchez P. (2023) Paragenesis and precipitation stages of Nb-Ta-oxide minerals in phosphorus-rich rare-element pegmatites (Buranga dike, Rwanda). *Am. Mineral.* **108**, 277–296.

Prado Araujo F., Martins L., Pereira G. de S. and Janasi V. de A. (2020) Inhandjara topaz leucogranite: A late rare metal-mineralized stock within the A-type Itu batholith, SE Brazil. *Journal of South American Earth Sciences* **101**, 102623.

Raimbault L., Cuney M., Azencott C., Duthou J. L. and Joron J. L. (1995) Geochemical evidence for a multistage magmatic genesis of Ta-Sn-Li mineralization in the granite at Beauvoir, French Massif Central. *Econ. Geol.* **90**, 548–576.

Rao C., Wang R., Yang Y., Hatert F., Xia Q., Yue X. and Wang W. (2017) Insights into post-magmatic metasomatism and Li circulation in granitic systems from phosphate minerals of the Nanping No. 31 pegmatite (SE China). *Ore Geol. Rev.* **91**, 864–876.

Roda-Robles E., Galliski M. Á., Roquet B., Hatert F. and de Parseval P. (2012a) Phosphate nodules containing two distinct assemblages in the Cema granitic pegmatite, San Luis province, Argentina: Paragenesis, composition and significance. *Can. Mineral.* **50**, 913–931.

Roda-Robles E., Pesquera A., Gil-Crespo P. P. and Torres-Ruiz J. (2012b) From granite to highly evolved pegmatite: A case study of the Pinilla de Fermoselle granite-pegmatite system (Zamora, Spain). *Lithos* **153**, 192–207.

Roda-Robles E., Vieira R., Pesquera A. and Lima A. (2010) Chemical variations and significance of phosphates from the Fregeneda-Almendra pegmatite field, Central Iberian Zone (Spain and Portugal). *Mineral. Petrol.* **100**, 23–34.

Roda E., Pesquera A., Fontan F. and Keller P. (2004) Phosphate mineral association in the Cañada pegmatite (Salamanca, Spain): Paragenetic relationships, chemical compositions, and implications for pegmatite evolution. *Am. Mineral.* **89**, 110–125.

Roedder E. (1984) Fluid Inclusions. *Reviews in Mineralogy* **12**, 644 p.

Ruiz-Agudo E., Putnis C. V. and Putnis A. (2014) Coupled dissolution and precipitation at mineral-fluid interfaces. *Chem. Geol.* **383**, 132–146.

Shaw R. A., Goodenough K. M., Deady E., Nex P., Ruzvidzo B., Rushton J. C. and Mounteney I. (2022) The Magmatic–Hydrothermal Transition in Lithium Pegmatites: Petrographic and Geochemical Characteristics of Pegmatites from the Kamativi Area, Zimbabwe. *Can. Mineral.* **60**, 1–31.

Shigley J. E. and Brown G. E. (1986) Lithiophilite formation in granitic pegmatites: a reconnaissance experimental study of phosphate crystallization from hydrous aluminosilicate melts. *Am. Mineral.* **71**, 356–366.

Siegel K., Wagner T., Trumbull R. B., Jonsson E., Matalin G., Wälle M. and Heinrich C. A. (2016) Stable isotope (B, H, O) and mineral-chemistry constraints on the magmatic to hydrothermal evolution of the Varuträsk rare-element pegmatite (Northern Sweden). *Chem. Geol.* **421**, 1–16.

Simmons W. B. and Webber K. L. (2008) Pegmatite genesis: state of the art. *Eur. J. Mineral.* **20**, 421–438.

Sirbescu M.-L. C. and Nabelek P. I. (2003a) Crustal melts below 400 °C. *Geology* **31**, 685–688.

Sirbescu M.-L. C. and Nabelek P. I. (2003b) Crystallization conditions and evolution of magmatic fluids in the Harney Peak Granite and associated pegmatites, Black Hills, South Dakota - Evidence from fluid inclusions. *Geochim. Cosmochim. Acta* **67**, 2443–2465.

Sirbescu M.-L. C., Schmidt C., Veksler I. V., Whittington A. G. and Wilke M. (2017) Experimental crystallization of undercooled felsic liquids: Generation of pegmatitic texture. *J. Petrol.* **58**, 539–568.

Tack L., Wingate M. T. D., De Waele B., Meert J., Belousova E., Griffin B., Tahon A. and Fernandez-Alonso M. (2010) The 1375Ma "Kibaran event" in Central Africa: Prominent emplacement of bimodal magmatism under extensional regime. *Precambrian Research* **180**, 63–84.

Thomas R. and Davidson P. (2015) Comment on "A petrologic assessment of internal zonation in granitic pegmatites" by David London (2014). *Lithos* **212**–**215**, 462–468.

Thomas R. and Davidson P. (2016) Revisiting complete miscibility between silicate melts and hydrous fluids, and the extreme enrichment of some elements in the supercritical state - Consequences for the formation of pegmatites and ore deposits. *Ore Geol. Rev.* **72**, 1088–1101.

1175 Thomas R. and Davidson P. (2013) The missing link between granites and granitic pegmatites.
1176 *Journal of Geosciences* **58**, 183–200.
1177 Thomas R. and Webster J. D. (1999) Characteristics of berlinite from the Ehrenfriedersdorf
1178 pegmatite, Erzgebirge, Germany. *Z. geol. Wiss.* **27**, 443–454.
1179 Thomas R., Webster J. D. and Heinrich W. (2000) Melt inclusions in pegmatite quartz: Complete
1180 miscibility between silicate melts and hydrous fluids at low pressure. *Contrib. Mineral. Petrol.*
1181 **139**, 394–401.
1182 Varlamoff N. (1972) Central and West African rare-metal granitic pegmatites, related aplites, quartz
1183 veins and mineral deposits. *Mineralium Deposita* **7**, 202–216.
1184 Varlamoff N. (1961) Matériaux pour l'étude des pegmatites du Congo et du Ruanda. IV. Pegmatites
1185 à amblygonite et à spodumène et pegmatites fortement albitisées à spodumène et à cassitérite de
1186 la région de Katumba (Ruanda). *Annales de la Société Géologique de Belgique* **84**, 257-278. (in
1187 French).
1188 Vasyukova O. and Williams-Jones A. E. (2014) Fluoride-silicate melt immiscibility and its role in
1189 REE ore formation: Evidence from the Strange Lake rare metal deposit, Québec-Labrador,
1190 Canada. *Geochim. Cosmochim. Acta* **139**, 110–130.
1191 Veksler I. V. (2004) Liquid immiscibility and its role at the magmatic-hydrothermal transition: A
1192 summary of experimental studies. *Chem. Geol.* **210**, 7–31.
1193 Veksler I. V., Dorfman A. M., Dulski P., Kamenetsky V. S., Danyushevsky L. V., Jeffries T. E. and
1194 Dingwell D. B. (2012) Partitioning of elements between silicate melt and immiscible fluoride,
1195 chloride, carbonate, phosphate and sulfate melts, with implications to the origin of
1196 natrocarbonatite. *Geochim. Cosmochim. Acta* **79**, 20–40.
1197 Veksler I. V. and Thomas R. (2002) An experimental study of B-, P- and F-rich synthetic granite
1198 pegmatite at 0.1 and 0.2 GPa. *Contrib. Mineral. Petrol.* **143**, 673–683.
1199 Veksler I. V., Thomas R. and Wirth R. (2003) Crystallization of $AlPO_4$-SiO_2 solid solutions from
1200 granitic melt and implications for P-rich melt inclusions in pegmatitic quartz. *Am. Mineral.* **88**,
1201 1724–1730.

1202 Webster J. D. (1997) Exsolution of magmatic volatile phases from Cl-enriched mineralizing granitic
1203 magmas and implications for ore metal transport. *Geochim. Cosmochim. Acta* **61**, 1017–1029.
1204 Webster J. D., Thomas R., Rhede D., Förster H. J. and Seltmann R. (1997) Melt inclusions in quartz
1205 from an evolved peraluminous pegmatite: Geochemical evidence for strong tin enrichment in
1206 fluorine-rich and phosphorus-rich residual liquids. *Geochim. Cosmochim. Acta* **61**, 2589–2604.
1207 Whitworth M. P. and Rankin A. H. (1989) Evolution of fluid phases associated with lithium
1208 pegmatites from SE Ireland. *Mineral. Mag.* **53**.
1209 Włodek A., Grochowina A., Golebiowska B. and Pieczka A. (2015) A phosphate-bearing pegmatite
1210 from Lutomia and its relationships to other pegmatites of the Góry Sowie Block, southwestern
1211 Poland. *Journal of Geosciences* **60**, 45–72.
1212 Yardley B. W. D. (2005) 100th Anniversary Special Paper: Metal concentrations in crustal fluids and
1213 their relationship to ore formation. *Econ. Geol.* **100**, 613–632.
1214 Zajacz Z., Halter W. E., Pettke T. and Guillong M. (2008) Determination of fluid/melt partition
1215 coefficients by LA-ICPMS analysis of co-existing fluid and silicate melt inclusions: Controls on
1216 element partitioning. *Geochim. Cosmochim. Acta* **72**, 2169–2197.
1217